REPORT DOCUMENTATION PAGE

The public reporting burden for this collection of information is estimated to average 1 hour per response, including the time for reviewing instructions, searching existing data sources, gathering end maintaining the data needed, end completing end reviewing the collection of information. Send comments regarding this burden estimate or eny other aspect of this collection of information, including suggestions for reducing the burden, to the Department of Defense, Executive Service Directorate (0704-0188). Respondents should be aware thet notwithstanding eny other provision of law, no person shell be subject to eny penalty for failing to comply with e collection of information if It does not display e currently valid OMB control number.
PLEASE DO NOT RETURN YOUR FORM TO THE ABOVE ORGANIZATION.

1. REPORT DATE (DD-MM-YYYY)	2. REPORT TYPE	3. DATES COVERED (From - To)
28-06-2010	Final report	February 2007-February 2010

4. TITLE AND SUBTITLE	5a. CONTRACT NUMBER
YIP - Low-Order Models of Highly-Irregular Surface Roughness and Their Impact on Wall Turbulence	
	5b. GRANT NUMBER
	FA9550--07-1-0129
	5c. PROGRAM ELEMENT NUMBER
6. AUTHOR(S)	5d. PROJECT NUMBER
Ricardo Mejia-Alvarez and Kenneth T. Christensen	
	5e. TASK NUMBER
	5f. WORK UNIT NUMBER

7. PERFORMING ORGANIZATION NAME(S) AND ADDRESS(ES)	8. PERFORMING ORGANIZATION REPORT NUMBER
University of Illinois 506 S. Wright St., 364 Henry Administration Bldg. Urbana, IL 61801	

9. SPONSORING/MONITORING AGENCY NAME(S) AND ADDRESS(ES)	10. SPONSOR/MONITOR'S ACRONYM(S)
USAF, AFRL AF Office of Scientific Research *RSA* Dr. John Schmisseur, Program Manager 875 N. Randolph St., Rm 3112 Arlington, VA 22203	AFOSR
	11. SPONSOR/MONITOR'S REPORT NUMBER(S)

12. DISTRIBUTION/AVAILABILITY STATEMENT
Approved for public release

20100916280

13. SUPPLEMENTARY NOTES

14. ABSTRACT
This effort explored the impact of topographical scales present within irregular surface roughness on a turbulent boundary layer. Low-order representations of a surface replicated from a turbine blade damaged by deposition of foreign materials were generated using singular value decomposition to decompose the complex topography into a set of basis functions of decreasing importance to the original ("full") surface. The low-order surface models were then formed by truncating the basis functions at the first 5 and 16 modes (containing 71% and 95% of the full surface content, respectively), so that only the largest-scale topographical features were included. Physical replications of these surfaces were rapid prototyped and particle-image velocimetry was used to measure the flow over these surfaces in the streamwise—wall-normal plane and in a streamwise—spanwise plane deep within the roughness sublayer. A 16-mode model of the full surface faithfully reproduced most of the characteristics of flow over the full surface for both developing and developed flow conditions. However, both models failed to reproduce important details of the Reynolds-shear-stress-producing events within the roughness sublayer. The final report details these observations.

15. SUBJECT TERMS
surface roughness; wall turbulence; realistic roughness

16. SECURITY CLASSIFICATION OF:			17. LIMITATION OF ABSTRACT	18. NUMBER OF PAGES	19a. NAME OF RESPONSIBLE PERSON
a. REPORT	b. ABSTRACT	c. THIS PAGE			Kenneth T. Christensen
			UU	43	19b. TELEPHONE NUMBER (Include area code) 217-333-0966

Final Report for AFOSR Grant FA9550-07-1-0129 Entitled "YIP–Low-Order Representations of Irregular Surface Roughness and Their Impact on Wall Turbulence"

R. Mejia-Alvarez[*] and K. T. Christensen[†]
Department of Mechanical Science and Engineering
University of Illinois at Urbana-Champaign
Urbana, IL 61801 USA

June 28, 2010

Abstract

This effort explored the impact of various topographical scales present within irregular surface roughness on a turbulent boundary layer. Low-order representations of a surface replicated from a turbine blade damaged by deposition of foreign materials were generated using singular value decomposition to decompose the complex topography into a set of topographical basis functions of decreasing importance to the original ("full") surface. The low-order surface models were then formed by truncating the full set of basis functions at the first 5 and 16 modes (containing 71% and 95% of the full surface content, respectively), so that only the largest-scale topographical features were included in the models while the finer-scale surface details were excluded. Physical replications of these surfaces were rapid prototyped and particle-image velocimetry was used to measure the flow over these surfaces in the streamwise–wall-normal plane and in a streamwise–spanwise plane deep within the roughness sublayer. A 16-mode model of the full surface faithfully reproduced most of the characteristics of flow over the full surface for both developing and developed flow conditions. However, both models failed to reproduce important details of the Reynolds-shear-stress-producing events within the roughness sublayer.

1 Introduction

Roughness effects can play a crucial role in a variety of practical engineering systems, from internal flows such as those through oil and gas pipelines to external flows like those over the surfaces of turbine blades and heat exchangers. In some instances, surface roughness occurs in isolated regions of a flow surface meaning that the flow will be intermittently perturbed by one or more step changes in surface condition from smooth to rough and vice-versa. Such transitions in surface quality can inhibit the flow from attaining a self-similar state (termed developed flow herein). On the other hand, there are other applications for which surface roughness occurs consistently along the entire length of a flow surface of interest, meaning that its development may eventually attain self-similarity since the flow is not intermittently perturbed by step changes in surface quality. Regardless of the roughness scenario, it is of significant interest to understand the impact of surface roughness for improved modeling, prediction and eventually control of practical flow systems in the presence of such effects.

Indeed, many studies have addressed various aspects of surface-roughness effects on wall turbulence under both developing and developed conditions. However, despite the fact that

---

[*]Ph.D. Student
[†]Principal Investigator

the surface quality in engineering systems can be highly irregular due to multiple damage mechanisms and can vary from aerodynamically smooth prior to deployment to significantly roughened over time due to cumulative degradation, most of these efforts employed idealized roughness, like sand grain, woven mesh and patterned arrays of rough elements. While such topographies are relatively easy to realize in a laboratory setting, their ordered character and narrow spectrum of scales are often counter to the surface characteristics of practical flow systems. For example, turbine blades suffer significant surface degradation over their deployment lifetime due to a multitude of mechanisms, including deposition of foreign materials, pitting and spallation. Close inspection of aged turbine blades reveals surface degradation marked by a broad range of topographical scales as well as a relatively high intermittency of occurrence [1, 2]. Other examples of irregular roughness include accumulation of algae and barnacles on the exterior surfaces of submarines and ships [3] as well as cumulative erosion on the blades of wind turbines operating near the sea. In all of these examples, single-scale roughness arranged in an ordered manner will likely not be representative of the rich topographies encountered in practice. Such differences have been known for decades, most notably discrepancies in friction factor in the transitionally rough regime between Nikuradse's results for monodisperse sand-grain roughness [4] and Colebrook's relationship based on "industrial" roughness containing a broad range of topographical scales [5, 6]. More recently, Bons [2] found that classical scalings for skin friction over rough walls, derived for flows over idealized roughness, do not hold for some flows over scaled turbine-blade roughness. As such, an understanding of idealized roughness effects may not properly extrapolate to the more practical case of highly-irregular surface roughness.

It is well-documented that an abrupt change in surface conditions from smooth to rough leads to the formation of an internal roughness layer that grows in thickness with distance downstream [7]. Studies of idealized roughness indicate an overshoot in the wall shear stress just downstream of this step change in surface condition [8, 9]. In addition, a significant enhancement in the production of turbulence is noted in the immediate vicinity of the roughness which yields higher values of both Reynolds normal and shear stresses within the internal layer compared to the upstream smooth-wall flow [8, 9, 10]. In contrast, the flow outside this layer remains relatively undisturbed. Such roughness effects diffuse away from the wall with increasing downstream distance from the step change in surface condition until the internal layer eventually engulfs the entire wall normal extent of the boundary layer and the flow approaches a self-similar (developed) state. Previous studies indicate that the precise growth in the thickness of the internal layer is tied to the details of the rough surface encountered [9]. Finally, roughness can also significantly reduce the spatial scales of the flow within the internal layer for developing flow [8]. With regard to more irregular roughness, Wu and Christensen [11] studied the impact of a short streamwise fetch of turbine-blade roughness due to spallation damage and marked by a broad range of topographical scales on incoming fully-developed, smooth-wall turbulent channel flow. This effort revealed both the formation of the expected internal layer upon transition from smooth- to rough-wall conditions as well as enhanced local Reynolds stresses within the internal layer of this developing flow due to large-scale topographical features.

For developed flow, wherein the internal layer has grown to engulf the entire boundary-layer thickness and the flow has attained a self-similar state, it is well-accepted that roughness governs the character of turbulence within the roughness sublayer ($3 - 5k$ away from the wall, where k is a measure of the roughness height). Outside the roughness sublayer, however, roughness may not have a direct impact on the flow as many studies of idealized roughness report that the turbulence behaves similarly to that of smooth-wall flow when properly scaled [12, 13, 14, 15, 16, 17, 18, 19, 20, 21]. These observations are in accordance with Townsend [22] who first hypothesized that at high Reynolds numbers (Re), the turbulent motions in the outer layer are independent of surface conditions and viscosity except for their role in setting the wall shear stress, τ_w (and hence the friction velocity, $u_\tau = [\tau_w/\rho]^{1/2}$, where ρ is the fluid density) and the boundary-layer thickness, δ. With respect to rough-wall flows, this hypothesis implies that if the

characteristic roughness height, k, is sufficiently small compared to δ then the direct impact of roughness is confined within the roughness sublayer. Under such conditions, the turbulence in the outer layer is only indirectly influenced by roughness through its role in determining u_τ and δ [23]. Previous studies [24, 19] indicate that this scale separation as represented by δ/k must exceed 40–50 for outer-layer similarity to exist (where k is either taken to be the characteristic roughness height or the equivalent sand-grain height, k_s).

Outer-layer similarity has also been reported for turbulent flow over more practical roughness. For example, Allen *et al.* [25] studied turbulent pipe flow in the presence of a honed surface akin to the industrial-type roughness of Colebrook [6] and reported smooth- and rough-wall mean velocity defect profiles, streamwise turbulence intensity profiles, and streamwise velocity spectra that collapsed in the outer layer in accordance with Townsend's wall similarity hypothesis. Similarly, Wu and Christensen [26] reported that the turbulence statistics outside the roughness sublayer remain unaffected by roughness replicated from a turbine blade damaged by deposition materials (compared to smooth-wall flow) when one accounts for the increased drag at the surface when scaling the statistics (using u_τ and δ). This similarity was also found to extend to the average spatial structure of the flow through comparison of two-point velocity correlation coefficients outside the roughness sublayer. Thus, Townsend's hypothesis provides a simple means of predicting outer-layer behavior for rough-wall flows based simply on knowledge of u_τ and δ, though previous studies indicate that it may not be a universal characteristic of all developed rough-wall flows [27, 28, 29, 30]. Further, while the outer layer may not be directly influenced by the details of the roughness topography in question, such details will undoubtedly have a defining impact on the local flow behavior within the roughness sublayer. Thus, given the crucial importance topographical details can play in both developing and developed flows, and the fact that idealized roughness characterizations generally embody a rather restricted distribution of topographical scales, the effect of idealized roughness conditions upon wall-bounded turbulence may be insufficient for successful modeling and/or control of practical flows in the presence of irregular roughness.

Given the topographical complexity of realistic roughness, the relative impact that each topographical scale of an irregular surface has on the flow is certainly of interest. That is, are flows over irregular roughness predominantly governed by the impact of the largest roughness scales or do the finer surface features contribute in a meaningful way? Colebrook and White [5] recognized the importance of this issue in their studies of industrial roughness and reported an enhancement in pipe-flow friction factor with the addition of sandgrain roughness to larger roughness protrusions compared to flow over the larger protrusions alone. Schultz and Flack [31] compared the flow over uniform spheres and the same topography with the addition of finer-scale sandgrain roughness. They reported good agreement between the Reynolds stress profiles for flow over both surfaces throughout the boundary layer, indicating little effect of finer-scale roughness on the turbulence. However, as with the experiments of Colebrook and White [5], it is not clear how this study of two roughness scales of substantially different size translates to the case of practical roughness which is marked by a broad spectrum of topographical scales. With respect to more irregular roughness, Itoh *et al.* [32] measured turbulent flow over the fur surface of a seal which exhibited a riblet-like character, though both the amplitude and wavelength of these topographical features varied significantly in space. Itoh *et al.* [32] also made measurements of turbulent flow over a model of the seal fur that consisted of ordered riblets manufactured with the dominant amplitude and wavelength of the seal fur. Comparison of these results indicated a lack of consistency in the turbulence statistics for flow over the real seal surface and the model. These differences highlight the importance of topographical characteristics beyond simply the dominant amplitude and wavelength of the real surface in determining its impact on the flow. Finally, Johnson and Christensen [33] considered the development of low-order topographical models of roughness replicated from a turbine blade that contained deep recesses of varying size due to spallation damage. Model topographies were developed using

3

singular value decomposition (SVD) and short fetches of the models were fabricated and tested in turbulent channel flow in which the upstream smooth-wall flow was fully-developed. Under these developing, internal flow conditions, it was found that a model containing only the larger- and intermediate scales of the topography (10% of the total modes) adequately reproduced the single-point statistics of flow over the full surface within the internal layer formed by the abrupt transition from smooth to rough conditions.

The present contribution builds upon the initial efforts of Johnson and Christensen [33] by considering the development of low-order topographical models of a different highly-irregular surface roughness replicated from a turbine blade damaged by deposition of foreign materials. The ability of these models to reproduce the characteristics of flow over the original roughness was then assessed under both developing and developed flow conditions in a turbulent boundary layer. Singular value decomposition was used to decompose the highly-inhomogeneous surface topography into a set of basis functions of decreasing contribution to the overall topography. Only the most dominant of these basis functions were used to reconstruct the surface topography, meaning that a substantial fraction of the larger-scale surface features were included in the low-order models while the finer topographical details are neglected. Short and long streamwise fetches of these low-order representations were then fabricated and tested in a zero-pressure-gradient turbulent boundary layer to assess how well they reproduce the flow modifications generated by the full surface topography under both developing- and developed-flow conditions. Such comparisons are meant to reveal the relative importance of finer-scale roughness features compared to the most dominant roughness scales in the context of highly irregular roughness in an external flow arrangement.

2   Experiments

Particle-image velocimetry (PIV) in the streamwise–wall-normal $(x - y)$ plane and stereo PIV in a streamwise–spanwise plane deep within the roughness sublayer at $y = 0.047\delta$ were used to study the impact of low-order models of surface roughness replicated from a turbine blade damaged by deposition of foreign materials on a zero-pressure-gradient turbulent boundary layer at $\mathrm{Re}_\theta \equiv U_e\theta/\nu \approx 15\,000$ for developing flow and $13\,000$ for developed flow, where U_e is the free-stream velocity, θ is the momentum thickness and ν is the kinematic viscosity of the fluid. All measurements were made in an Eiffel-type, open circuit, boundary-layer wind tunnel with a documented turbulence intensity of 0.16% in the free stream [34]. The boundary-layer plate utilized in all of the experiments consists of two 3 m-long by 1 m-wide flat plates suspended above the bottom wall of the tunnel that are smoothly joined at the streamwise center of the test section.

2.1   Roughness

The rough-wall conditions considered herein were derived from one of the surfaces characterized by Bons et al. [1] and subsequently used by Bons [2] to study bulk skin friction and heat transfer characteristics over turbine-blade roughness (surface 4 in Bons [2]). It should be noted that the original profilometry measurements of this damaged turbine-blade surface by Bons et al. [1] yielded roughness heights on the order of tens to hundreds of microns. Therefore, in order to generate fully-rough conditions for the relatively thick boundary layers generated by the flow facility employed ($\delta \sim 100\,\mathrm{mm}$) at the Re_θ considered herein, the original profilometry information was scaled up in all three dimensions to yield a topographical condition with $k = 4.25\,\mathrm{mm}$ (Following Bons [2], the characteristic roughness height, k, is taken to be the average peak-to-valley height.). The topographical features of this surface, shown in figure 1(a), are elliptical in shape, are generally aligned in the streamwise direction and are attributable to cumulative deposition of foreign materials on the blade surface. However, a broad range of topographical
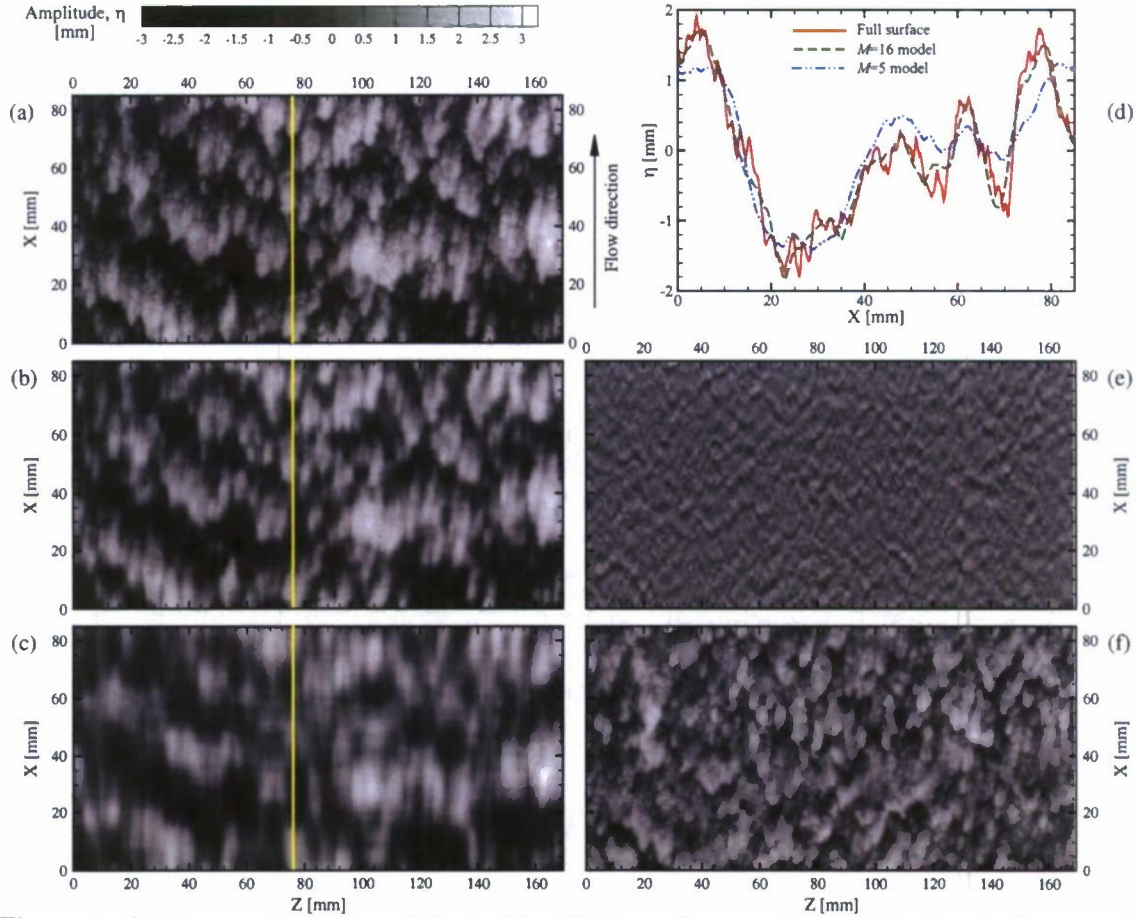
4

Figure 1: (a) Topographical map of the turbine-blade roughness under consideration in the present effort (the "full" surface). (b,c) Low-order representations of the full surface generated with the first 16 and 5 SVD modes, respectively. (d) Streamwise profiles of roughness amplitude for the full surface and the two low-order representations coincident with the lines in (a)–(c) which demarcate the spanwise position of the streamwise–wall-normal PIV measurement plane in the present experiments. (e,f) Residual topographical maps for the 16- and 5-mode topographical models, respectively.

scales is also clearly evident in this surface. Of particular interest, the general characteristics of this surface are representative of surface roughness encountered in many practical flows of interest but are quite distinct from the "idealized" roughness typically studied in the laboratory, including sand grain, mesh and ordered arrays of elements. Given that the boundary layers under consideration have thicknesses of approximately 100 mm, the full-surface condition gives $\delta/k \sim 24 - 30$ (δ is taken as the wall-normal position where the mean streamwise velocity equals 99% of the free-stream velocity for all cases). Further, the root-mean-square (RMS) roughness height, $k_{\rm rms}$, for the full surface is 1.0 mm while its skewness and flatness are 0.16 and 2.27, respectively. For reference, a long fetch of this surface was studied by Wu and Christensen [35] and outer-layer similarity was observed in all single- and multi-point statistics.

The low-order reconstructions of this surface were devised using SVD of the fluctuating topography about the mean elevation. This methodology is akin to proper orthogonal decomposition (POD) as it provides an optimal basis for describing an inhomogeneous signal of interest (Only the details of SVD pertinent to the present application are presented. The reader is directed to Chatterjee [36], for example, for a more detailed discussion). To begin, the fluctuating

surface elevation of the full surface, $\eta_{\text{full}}(x, z)$, shown in figure 1(a) can be decomposed as

$$\eta(x, z) = \sum_{j=1}^{L} a_j \phi_j(x, z), \tag{1}$$

where the a_j's are coefficients of the expansion, the ϕ_j's represent orthogonal basis functions and L is the total number of basis functions. Using this decomposition, one can approximate the fluctuating surface elevation of the full surface as

$$\eta_{\text{full}}(x, z) \approx \eta_{\text{low}}^{M}(x, z) = \sum_{j=1}^{M} a_j \phi_j(x, z), \tag{2}$$

where η_{low}^{M} is referred to as the low-order (or reduced-order) representation of η_{full} based on only the first M ($< L$) modes of the decomposition. Therefore, some detail of the original surface is lost in this reconstruction.

The basis functions and coefficients of the expansion in eqn. (1) are determined using SVD. One can write the topographical information contained in $\eta_{\text{full}}(x, z)$ in the form of a matrix $\mathbf{A}$ and this matrix can be decomposed by SVD as

$$\mathbf{A} = \mathbf{U} \boldsymbol{\Sigma} \mathbf{V}^T, \tag{3}$$

where $\mathbf{U}$ and $\mathbf{V}$ are orthogonal matrices and $\boldsymbol{\Sigma}$ is a diagonal matrix containing the singular values of $\mathbf{A}$, α_n, arranged in decreasing value. Relating this method back to POD, the squares of the singular values, $\lambda_j = \alpha_j^2$, represent the eigenvalues of $\mathbf{A}\mathbf{A}^T$ or $\mathbf{A}^T\mathbf{A}$ while the columns of $\mathbf{U}$ and $\mathbf{V}$ are related to the eigenvectors of $\mathbf{A}\mathbf{A}^T$ or $\mathbf{A}^T\mathbf{A}$, respectively [36]. Built-in SVD functions in *Matlab* are used to determine $\mathbf{U}$, $\boldsymbol{\Sigma}$ and $\mathbf{V}$ which yielded a total of $L = 383$ modes for the full-surface topography of figure 1(a).

As described in Johnson and Christensen [33], the low-order representations of the surface elevation can be realized by truncating the singular values in $\boldsymbol{\Sigma}$ at mode M while singular values $M + 1$ through L are rendered zero. This modified singular-value matrix, $\boldsymbol{\Sigma}_M$, was then utilized to compute the low-order topographical representation, $\mathbf{A}_M$, as

$$\mathbf{A}_M = \mathbf{U} \boldsymbol{\Sigma}_M \mathbf{V}^T, \tag{4}$$

where $\mathbf{A}_M$ embodies η_{low}^{M} from eqn. (2). Since the singular values are arranged in descending order, the first M modes represent the most dominant modes of the surface elevation which, as is the case in POD, embody the larger spatial scales of the original topography. Further, as described in Johnson and Christensen [33], the RMS roughness height for an M-order model, k_M^{rms}, can be related to $k_{\text{full}}^{\text{rms}}$ as

$$(k_M^{\text{rms}})^2 = (k_{\text{full}}^{\text{rms}})^2 \frac{\sum_{j=1}^{M} \lambda_j}{\sum_{j=1}^{L} \lambda_j}. \tag{5}$$

Thus, we refer to the ratio on the right-hand side of eqn. (5) as the fractional surface content (FSC) of the low-order representation containing the first M modes as it provides a measure of the detail from the full surface retained in the M-order reconstruction.

Replicas of the full surface as well as the low-order models were fabricated using a rapid-prototyping method based on powder deposition with a spatial resolution of $80\,\mu$m as described in Wu and Christensen [35]. The full surface was fabricated, in addition to two low-order models constructed from the most dominant modes of the aforementioned decomposition: $M = 5$ and $M = 16$ ($M = 5$ implies only the first five basis functions are included while $M = 16$ indicates that the first sixteen basis functions are included in the reconstruction). The low-order models

Surface	FSC	k (mm)	k_{rms} (mm)	Skewness	Flatness
Full surface	1	4.25	1.0	0.16	2.27
$M = 16$ model	0.95	4.09	0.975	0.20	2.34
$M = 5$ model	0.71	3.66	0.84	0.24	2.82

Table 1: Various characteristics of the rough surfaces under consideration.

of the full surface are hereafter referred to by the highest-order mode, M, included in the low-order reconstruction. Figures 1(b) and 1(c) present topographical maps of the $M = 16$ ($k^{\text{rms}}_{M=16} = 0.975\,\text{mm}$) and $M = 5$ ($k^{\text{rms}}_{M=5} = 0.84\,\text{mm}$) low-order representations, respectively, which clearly illustrate the increased topographical detail embodied in the models with increasing modal content. In particular, the $M = 16$ model [figure 1(b)] bears a striking resemblance to the full surface [figure 1(a)] which includes all 383 modes. For reference, the FSC of the $M = 16$ reconstruction is 0.95 ($k^{\text{rms}}_{M=16} = 0.975 k^{\text{rms}}_{\text{full}}$), meaning nearly all of the topographical detail of the full surface is embodied in this model. In contrast, the low-order representation containing the first five modes only loosely reflects the largest-scale surface defects present in the full surface which is justified by its relatively low FSC of 0.71 ($k^{\text{rms}}_{M=5} = 0.81 k^{\text{rms}}_{\text{full}}$). The average characteristics of each roughness case are summarized in table 1.

Since the low-order surface representations presented in figures 1(b) and 1(c) were generated by truncating the series representation in eqn. (1) at mode M, there exists a set of residual topographical modes from $M + 1$ to L that represent the surface content excluded in a low-order representation given by M. One can reconstruct the residual surface features embodied in these excluded modes for a given low-order representation M by computing its associated residual topographical field, η^M_{res}, as

$$\eta^M_{\text{res}}(x, z) = \eta_{\text{full}}(x, z) - \eta^M_{\text{low}}(x, z) = \sum_{j=M+1}^{L} a_j \phi_j(x, z). \tag{6}$$

Figures 1(e) and 1(f) present topographical maps of these residual fields for the $M = 16$ and $M = 5$ low-order reconstructions. The contour levels in these maps are consistent with those employed in the maps of the low-order representations themselves in order to facilitate direct comparison. As one would expect, a significant amount of the full-surface content is apparent in the residual field for the $M = 5$ case [figure 1(f)], as its spatial characteristics are quite consistent with the overall character of the full surface. This observation is consistent with the fact that the $M = 5$ low-order model contains only 71% of the full surface content, meaning that the residual field contains a not insignificant amount of information of the full surface (29%). In contrast, inclusion of 11 additional modes in the $M = 16$ case yields a residual topographical field [figure 1(e)] that bears little resemblance to the full surface. Instead, the $M = 16$ residual field is marked by weak, smaller-spatial-scale fluctuations in surface topography. The dominance of smaller-spatial-scale topographical fluctuations in this residual field is consistent with the fact the higher-order modes generated by SVD embody the contributions of smaller-scale spatial features.

Finally, figure 1(d) presents streamwise profiles of the full-surface roughness as well as the two low-order representations coincident with the lines in figures 1(a)–(c). These lines demarcate the spanwise position of the streamwise–wall-normal measurement plane for the PIV experiments presented herein. These profiles provide a more quantitative comparison of the low-order surface models to the full surface. This direct comparison highlights the finer-scale details that are excluded in the low-order representations, particularly in the case of the 5-mode model which only captures the larger-wavelength features of the full surface. In contrast, the 16-mode model provides a much more accurate description of the full surface, though loss of smaller-wavelength information in this model is still quite apparent. In particular, the large-
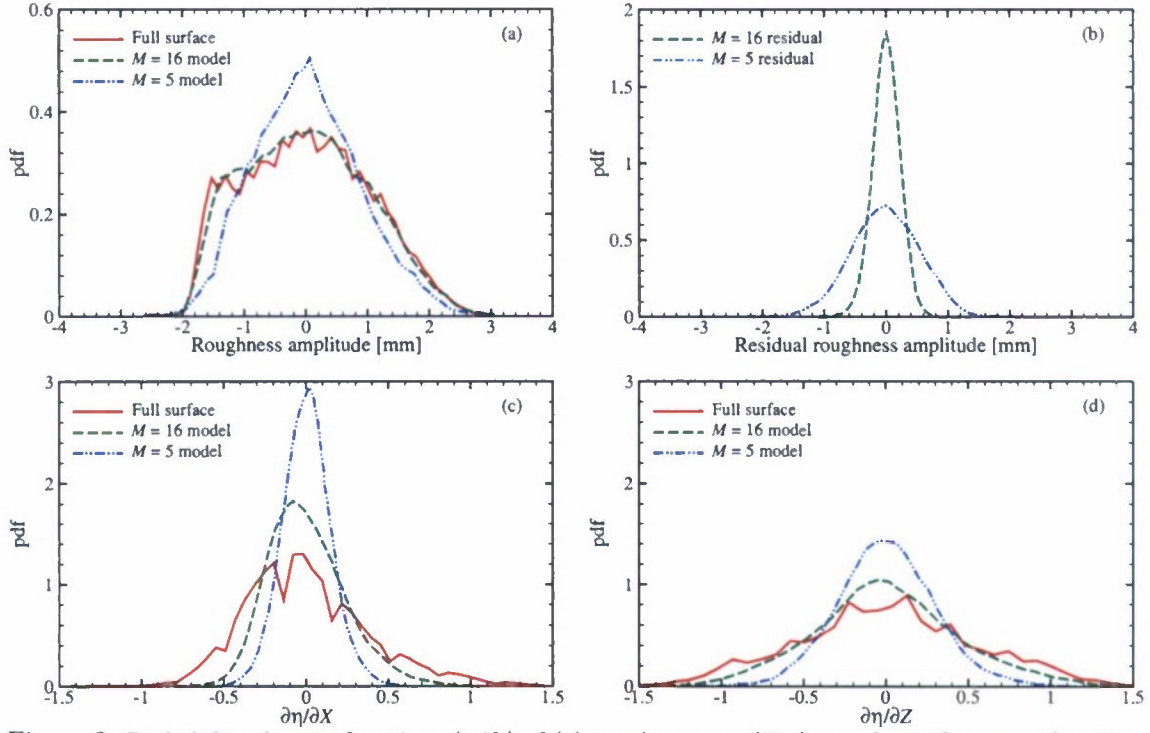
Figure 2: Probability density functions (pdfs) of (a) roughness amplitude, η, about the mean elevation, (b) residual roughness amplitude about the mean elevation, (c) streamwise surface gradient, $\partial\eta/\partial x$, and (d) spanwise surface gradient, $\partial\eta/\partial z$.

scale protrusions of the 16-mode model appear much smoother than those of the full surface which tend to contain more jagged smaller-scale detail. These similarities and differences are also reflected in figure 2(a) which presents probability density functions (pdfs) of roughness amplitude about the mean elevation for each surface case. The low-pass-filtering effect of the low-order reconstructions is apparent when comparing the pdf of roughness amplitude for the $M = 5$ model with that of the full surface. Removal of the finer scales embodied in the higher-order SVD modes effectively smooths the full-surface topography, though the $M = 16$ model captures the overall topographical trends of the full surface quite well. The pdfs of the residual modes for the $M = 5$ and $M = 16$ cases are presented in figure 2(b) and confirm that significant intermediate- and fine-scale detail of the surface is lost in the $M = 5$ case ($\sim \pm 1.5\,\text{mm}$) while the pdf for the residual roughness amplitudes for the $M = 16$ case is much narrower ($\sim \pm 0.5\,\text{mm}$). This filtering effect of truncation is most apparent, however, in pdfs of the streamwise and spanwise surface gradients, $\partial\eta/\partial x$ and $\partial\eta/\partial z$, presented in figures 2(c) and 2(d), respectively. Truncation of the higher-order modes clearly reduces the spatial gradients of the topography, most notably in the case of the $M = 5$ model, though the $M = 16$ model also deviates from the full-surface behavior much more than is discernable from the roughness amplitude pdfs. These trends therefore highlight the fact that the higher-order SVD modes not only embody smaller-scale elements of the full surface but also contribute to the larger-scale protrusions themselves, particularly the jagged edges of these protrusions as is notable in figure 1(d).

To facilitate testing, the aforementioned printer was used to construct replicas of each topography layer-by-layer with a maximum spatial footprint of $25 \times 30\,\text{cm}^2$ and a mean thickness of approximately 6 mm. In order to accommodate these roughness panels, the upstream half of the suspended flat plate in the wind tunnel was raised relative to the downstream half such that the mean elevation of the roughness was coincident with the upstream smooth wall. Since the original spatial footprint of the digitized topography was not sufficient to fill this large of an area, the topography was mirrored in both the streamwise and spanwise directions to achieve an

appropriate streamwise fetch of roughness [35]. Two different streamwise fetches of roughness were considered in this effort: 1 m (equivalently $\sim 10\delta$) and 3 m ($\sim 30\delta$) to facilitate the study of both developing and developed turbulent boundary layers. The boundary layers were tripped to initiate transition to turbulence at the leading edge of the suspended plate and grew over smooth-wall conditions for the first 3 m and 5 m for the developed and developing flow experiments, respectively, after which they encountered the roughness conditions considered herein. For reference, a 2 m-long smooth cast aluminum plate was laid along the downstream half of the boundary-layer plate to extend the upstream smooth-wall fetch an additional 2 m for the developing-flow cases, after which the flow encountered the 1 m-long patch of roughness. Since the initial boundary-layer development occurred over a smooth wall, this 1 m-long roughness scenario therefore represents the impact of short streamwise fetches of roughness on an incoming smooth-wall turbulent boundary layer. As such, one would expect the formation of an internal layer within the turbulent boundary layer wherein roughness effects are confined. In the 3 m-long roughness scenario, the flow is termed developed to reflect the fact that the internal roughness layer has grown to occupy the entire wall-normal extent of the turbulent boundary layer and a self-similar state is attained. The reproduction of over thirty individual roughness panels for each case was required to achieve a streamwise fetch of 1 m while an additional sixty panels per case were required to extend the streamwise fetch to 3 m. The panels were mounted to cast aluminum plates which were then laid along the downstream half of the wind tunnel. All measurements were made 0.8 m ($\sim 8\delta$) and 2.5 m ($\sim 25\delta$) downstream of the leading edge of the roughness for the developing- and developed-flow cases, respectively.

2.2 Streamwise–wall-normal plane PIV details

Over forty-five hundred statistically independent, two-dimensional velocity (u, v) fields were acquired by PIV in the streamwise–wall-normal (x, y) plane at the spanwise center of the tunnel for each surface condition to minimize sampling errors in the computed statistics. It should be noted that the streamwise and spanwise positions of this measurement plane were carefully maintained over the same roughness features for the developing- and developed-flow experiments, respectively, allowing a meaningful comparison of the flow statistics. The flow field was illuminated with a 500 μm-thick laser sheet generated by a pair of Nd:YAG lasers (200 mJ/pulse, 5 ns pulse duration) and a combination of spherical and cylindrical lenses. A high-energy mirror directed the laser sheet into the wind tunnel such that it was normal to the flow boundary and parallel to the flow direction. The flow was seeded with 1 μm olive oil droplets and time-separated images of the scattered light from the particles were captured with a 4k $\times$ 2.8k, 12-bit frame-straddle CCD camera over a field of view of $1.15\delta \times 0.8\delta$ (streamwise by wall-normal) and $1.4\delta \times \delta$ for the developing and developed flow experiments, respectively. The roughness at the measurement location was painted black to reduce reflections of laser light; however, the remaining unsuppressed reflections rendered measurements in the region $y \lesssim 0.06 - 0.1\delta$ impossible for the rough-wall cases. For reference, all rough-wall data presented herein is compared to data from a smooth-wall PIV experiment conducted at $\text{Re}_\theta = 11400$ ($\delta^+ = 3350$).

The pairs of PIV images were interrogated using a recursive, two-frame cross-correlation method. The sizes of the interrogation windows were chosen to maintain a consistent vector grid spacing between the various cases when scaled in inner units (i.e. by u_τ and ν) and the second window was offset by the bulk displacement to reduce errors associated with loss of image pairs. The grid spacing for all cases is $\Delta x^+ = \Delta y^+ = \Delta^+ \approx 18$ (where $(\cdot)^+$ denotes normalization in inner units) using the developed-flow viscous length scales for normalization. The resulting velocity vector fields were then validated using neighborhood mean and median comparisons to remove spurious vectors. On average, a valid vector yield of $> 97\%$ was achieved, minimizing the need for interpolation of holes. Finally, each velocity field was low-pass filtered with a narrow Gaussian filter to remove noise associated with frequencies larger than the sampling frequency
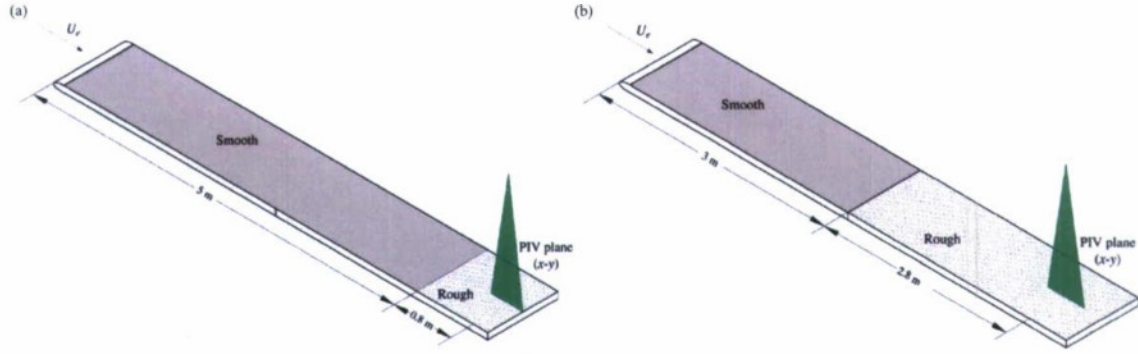
9

Figure 3: Schematics for (a) developing and (b) developed flow PIV measurements in the streamwise–wall-normal plane.

of the interrogation.

With regard to PIV measurement uncertainties, errors can arise from multiple sources. In particular, the random error associated with determining particle displacements in PIV is approximately 5% of the particle-image diameter [37]. In the present study, the mean particle-image diameter was approximately 2 pixels, yielding a random error of 0.1 pixels. Therefore, since the bulk displacements in the present experiments were 10–12 pixels, this random error is less than 1% of the full-scale velocity. In addition, bias errors can play an important role in the accuracy of PIV data. Bias due to loss of image pairs was minimized by utilizing a larger second interrogation window and a bulk window offset during interrogation of the PIV images. Bias errors due to the peak-locking effect were also minimized as the particle-image diameters exceeded 2 pixels [38, 39]. Finally, sampling errors in the statistics presented are small (approximately 1%) since averaging was performed over at least 1,250,000 statistically independent velocity samples per data point. As such, symbol size throughout accommodates the uncertainty bounds for each statistic presented.

Measurements were conducted under both developing and developed flow conditions for flow over the original roughness and the two low-order representations. Figure 3 presents a schematic of both surface scenarios whereby the developing-flow measurements were conducted 0.8 m ($\sim$ 8δ) downstream of the abrupt transition from smooth to rough conditions while the developed flow measurements were conducted 2.8 m ($\sim$ 28δ) downstream of this surface transition where self-similar conditions are assured. In both scenarios, the flow is allowed to develop into a smooth-wall self-similar turbulent boundary layer prior to reaching the rough surface.

2.3 Streamwise-spanwise plane stereo PIV details

For the stereo PIV measurements in the $x - z$ plane at $y = 0.047\delta$ (relative to the virtual origin for each rough-wall case), the two cameras were positioned approximately 1.5 m away from the measurement plane and imaged the flow through a transparent section in the wind-tunnel ceiling (see figure 4). The imaging paths of the cameras were rotated at $\pm 13°$ with respect to the wall-normal (y) axis. The laser light sheets were formed in a manner identical to that described earlier but were introduced into the tunnel through a glass sidewall while their orientations were carefully adjusted to ensure they remained parallel to the wall at $y = 0.047\delta$. Uniform image focus was ensured in both cameras across the entire field of view by satisfying the Scheimpflug condition. The pairs of images acquired by each camera were interrogated and validated independently in accordance with the methodology described above, resulting in pairs of instantaneous planar fields of two-dimensional particle displacements from the two cameras.
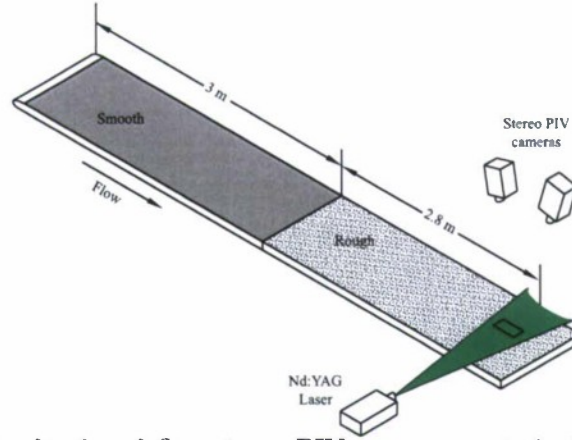
10

Figure 4: Schematic for developed flow stereo PIV measurements in the streamwise–spanwise plane at $y = 0.047\delta$.
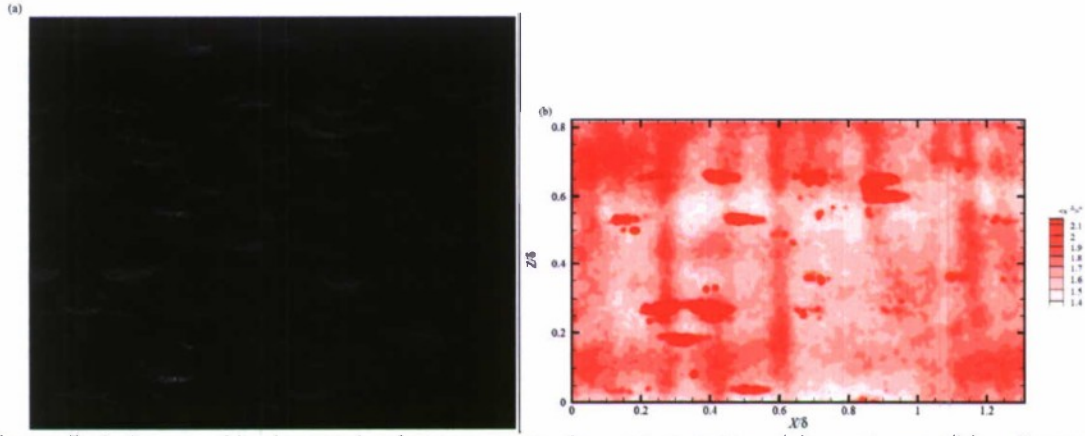

Figure 5: Influence of background reflections on single-point statistics. (a) raw image, (b) wall-normal Reynolds normal stress $< v'^2 >^+$.

These pairs of displacement fields were then recombined into instantaneous velocity fields using a mapping function generated via calibration of the imaging system. This calibration employed a dual-plane (1-mm separation) target containing white dots spaced at in-plane intervals of 10 mm over a 20 cm × 20 cm area. The use of this dual-plane target alleviated the need to physically translate the target in the depth direction through the lightsheet thickness. Instead, the target was carefully aligned in the field of view so that its mid-plane coincided with the laser lightsheet. With the target fixed at this location, an image was acquired from each camera, and these images were used to generate the mapping function via the least-squares method of Soloff *et al.* [40] using third-order polynomials for the in-plane coordinates and a first-order polynomial for the out-of-plane coordinate. A draw-back of this technique is that obtaining perfect alignment of the target with the laser lightsheet is virtually impossible. To overcome this problem, the self-calibration scheme originally proposed by Wieneke [41] was used to optimize the mapping function. The final mapping function was then used to reconstruct three-dimensional velocity vectors on the measurement plane from the pairs of two-dimensional particle displacements.

As these rough-wall experiments were begun, it was realized that an important challenge must be overcome. In particular, as the laser lightsheet was parallel to and within a few millimeters of the rough surfaces, surface reflections became a debilitating issue. While smooth-wall measurements were not tainted by such effects, the complex nature of the surface roughness under consideration led to intense reflections of laser light that was directed in all directions
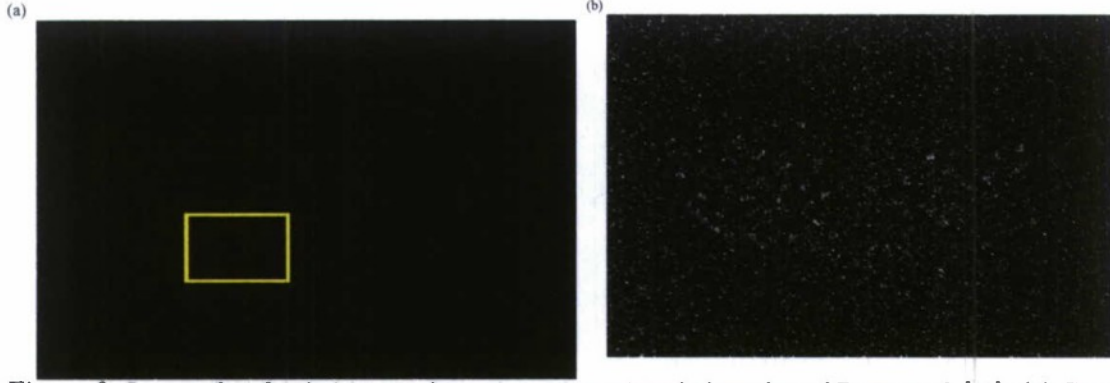
11

Figure 6: Image after fixed objects subtraction using original algorithm of Deen *et al.* [42]. (a) General view; (b) Zoom in on a former bright spot.

and thus appeared in the PIV images acquired. To highlight this issue, a sample PIV image for flow over the $M = 5$ model at $y = 0.047\delta$ is shown in figure 5 and the strong background reflections due to the largest roughness elements are obvious, particularly how intense these unwanted reflections are compared to the imaged light from the tracer particles. These background reflections unfortunately corrupt the PIV interrogation and induce strong bias in single-point statistics $[\langle v'^2 \rangle^+$ shown in figure 5(b)].

A solution to this type of background reflection problem was recently proposed by Deen *et al.* [42]. The basic idea of this method is to subtract frame B from frame A of instantaneous PIV realizations, which in theory would render the intensity of the fixed objects zero since they would scatter similar light in both frames (compared to the random nature of the scattered light from the moving tracer particles). To compensate for intensity differences due to disparity in the power of the two laser heads, the authors introduced an intensity normalization based on local values of minimum and maximum intensity. To sample for extreme values and normalize locally, they used an image spot of size larger that the average particle image but smaller than the intended PIV window size. The local normalization is then carried out as

$$N(\mathbf{x}) = \frac{I(\mathbf{x}) - I_{min}(\mathbf{x})}{I_{max}(\mathbf{x}) - I_{min}(\mathbf{x})}, \tag{7}$$

where $I(\mathbf{x})$ is the sliding local intensity and $I_{max}(\mathbf{x})$ and $I_{min}(\mathbf{x})$ are its maximum and minimum values, respectively. After normalizing, since the intensity values are bounded between 0 and 1, the two PIV frames can be subtracted from each other. After subtracting frame A from frame B, frame A will be recovered by extracting the positive values of intensity from the result while frame B will be recovered by extracting the negative values of intensity from the result and taking their absolute value. This approach worked well for the application presented by Deen *et al.* [42]; however, as can be observed in figure 6b, the normalization spot leaves a footprint in the formerly bright regions of the PIV images. Since the local maximum intensity may change from one frame to another due to particle displacement, the relative intensity of the background would also be different after local normalization. Thus, as proposed, this correction method is quite sensitive to extreme values.

To overcome this problem of extreme value sensitivity, we modified the method using an initial local normalization based on the local median and minimum intensity values as

$$N(\mathbf{x}) = \frac{I(\mathbf{x}) - I_{min}(\mathbf{x})}{I_{median}(\mathbf{x}) - I_{min}(\mathbf{x})}. \tag{8}$$

A frame subtraction was then applied followed by a local normalization according to equation (7). Finally, the intensity values were stretched to a 16-bit intensity range. The final result
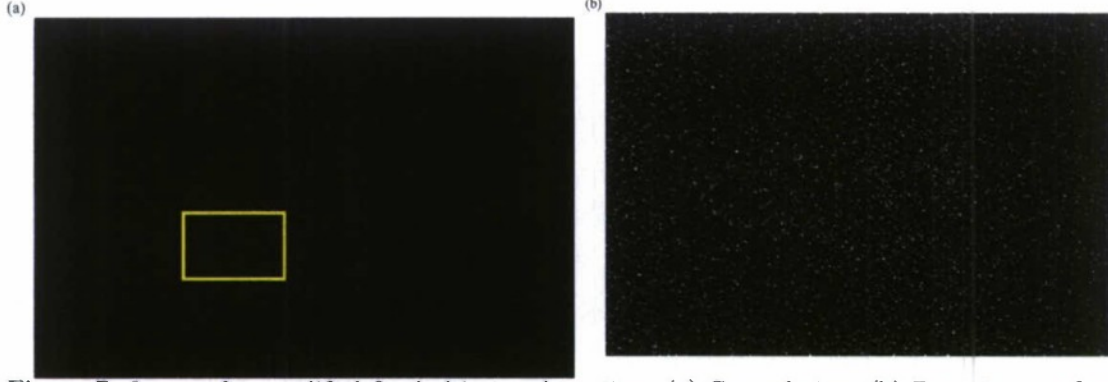
Figure 7: Image after modified fixed objects subtraction. (a) General view; (b) Zoom in on a former bright spot.

of this modified method is presented in figure 7 wherein the effect of the normalization spot is virtually non-existent which greatly reduced any bias due to background reflections. This modified background subtraction technique was employed for all of the stereo PIV measurements described herein, including the smooth-wall PIV images for consistency.

3   Analysis

The efficacy of the two different low-order representations in reproducing the characteristics of flow over the full surface under both developing- and developed-flow scenarios is evaluated by directly comparing various single-point statistics, including the mean velocity, the Reynolds normal stresses ($\langle u'^2 \rangle$ and $\langle v'^2 \rangle$) and the Reynolds shear stress (RSS; $\langle u'v' \rangle$). In all cases, the mean velocity profile was formed by ensemble-averaging all velocity realizations for a given case followed by line-averaging in the streamwise direction. The turbulence statistics considered herein were then computed in a similar manner using fluctuating velocity fields derived from the aforementioned mean velocity profiles.

Probability density functions are also used to contrast the instantaneous contributions to the RSS for flow over the two low-order models and the full surface. In this regard, the instantaneous $u'v'$ events that are averaged to generate the mean RSS profile can be formed by different combinations of u' and v' depending upon which quadrant of the $u' - v'$ plane a given instantaneous RSS event resides. In particular, negative contributions to $\langle u'v' \rangle$ are attributable to ejection (Q_2: $u' < 0$, $v' > 0$) and sweep (Q_4: $u' > 0$, $v' < 0$) events while positive contributions are generated by inward (Q_3: $u' < 0$, $v' < 0$) and outward (Q_1: $u' > 0$, $v' > 0$) interactions. To further explore the efficacy of the low-order models in reproducing the character of these individual quadrant events for flow over the full surface, quadrant analysis, as first proposed by Lu and Willmarth [43], is also applied to all cases. In quadrant analysis, the mean RSS at each wall-normal position is decomposed into contributions from four quadrants excluding a hyperbolic hole of size H as

$$\langle u'v' \rangle_Q(y; H) = \frac{1}{P} \sum_{j=1}^{P} u'(x_j, y)v'(x_j, y)I_Q(x_j, y; H), \qquad (9)$$

where P is the total number of velocity vectors at each wall-normal position and I_Q is the indicator function defined as

$$I_Q(x_j, y; H) = \begin{cases} 1, & \text{when } |u'(x_j, y)v'(x_j, y)|_Q \geq T \\ 0, & \text{otherwise}, \end{cases} \qquad (10)$$

13

Surface	Re_θ	U_e (m/s)	δ (mm)
Full surface	15 970	16.9	125.8
$M = 16$ model	15 540	16.8	120.9
$M = 5$ model	15 400	16.9	126.2

Table 2: Relevant experimental parameters for developing-flow experiments.

where T is a threshold that allows one to consider various magnitudes of instantaneous RSS events that contribute to the mean RSS. For developing flow this threshold is taken to be $T = H|\langle u'v'\rangle|_{\text{full}}^{\max}$ (the maximum in the mean RSS for the full-surface case) while for developed flow the threshold is defined as $T = H\sigma_u(y)\sigma_v(y)$ where $\sigma_u \equiv \langle u'^2\rangle^{1/2}$ and $\sigma_v \equiv \langle v'^2\rangle^{1/2}$ are RMS streamwise and wall-normal velocities, respectively. Here, the value H represents a threshold on the strength of the RSS-producing events considered in the analysis, with $H = 0$ allowing inclusion of all $u'v'$ events and increasing values of H allowing inclusion of only increasingly intense RSS-producing events. Using this thresholding of $u'v'$ events, one can also document the fraction of space, N_Q, they occupy as

$$N_Q(y; H) = \frac{\sum I_Q(y; H)}{P}. \tag{11}$$

Finally, two-point velocity correlation coefficients are compared under developed flow conditions to discern the impact of the low-order surface models on the spatial structure of the flow compared to flow over the full surface as well as the smooth-wall baseline. In this regard, previous studies of wall turbulence have established a strong linkage between the average spatial characteristics of these correlations and the dominant spatial structure of the flow. For the present streamwise–wall-normal PIV measurements, two-point velocity correlation coefficients of the form

$$\rho_{ij}(\Delta x, y; y_{\text{ref}}) = \frac{\langle u_i'(x, y_{\text{ref}})u_j'(x + \Delta x, y)\rangle}{\sigma_i(y_{\text{ref}})\sigma_j(y)}, \tag{12}$$

where σ_i and σ_j are the root-mean-square (RMS) velocities of the ith and j^{th} velocity components, are computed for the streamwise and wall-normal velocity components yielding three correlation coefficients ρ_{uu}, ρ_{vv} and ρ_{uv}. For reference, previous studies indicate fair similarity in these correlation coefficients for smooth- and rough-wall flow outside the roughness sublayer, though a shortening in the streamwise extent of ρ_{uu} has been reported for both idealized [44, 21] and irregular [26] roughness that can extend well beyond the roughness sublayer. Nonetheless, such similarity is consistent with Townsend's hypothesis and indicates relatively little impact of roughness on the spatial structure of the outer layer.

4 Streamwise–Wall-Normal Plane Measurements

4.1 Developing Flow

This section presents analysis of the PIV datasets acquired 0.8 m ($\sim 8\delta$) downstream of the leading edge of the roughness, meaning that roughness effects are confined within an internal layer initiated at the abrupt transition from smooth- to rough-wall conditions. Table 2 summarizes the relevant details of these experiments.

4.1.1 Mean velocity

Figure 8 presents the mean streamwise velocity profiles for the various surfaces under developing flow conditions. A deficit in the mean velocity is evident for the rough-wall cases compared to the smooth-wall profile. The wall-normal extent of this deficit, which can be interpreted as an
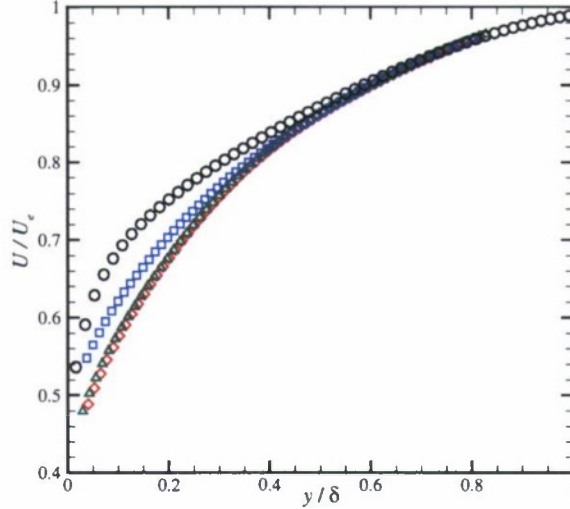
Figure 8: Mean velocity profiles in outer units (normalized with U_e and δ) for developing flow. Not all data points shown for clarity. ○: Smooth; □: $M = 5$ model; △: $M = 16$ model; ◇: Full surface.
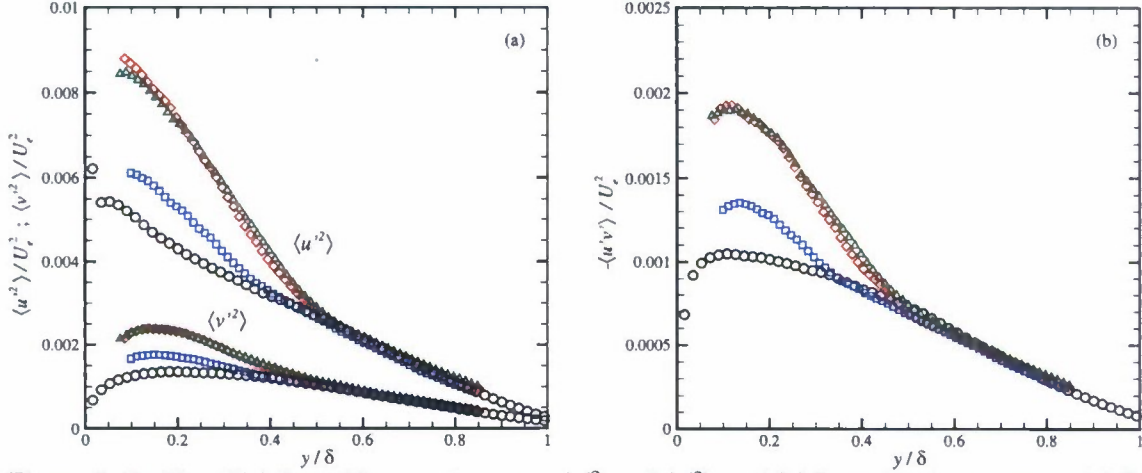

Figure 9: Profiles of (a) Reynolds normal stresses, $\langle u'^2 \rangle$ and $\langle v'^2 \rangle$, and (b) Reynolds shear stress, $-\langle u'v' \rangle$, for developing flow. Not all data points shown for clarity. ○: Smooth; □: $M = 5$ model; △: $M = 16$ model; ◇: Full surface.

internal layer within which roughness directly impacts the flow, is surface-dependent, with the full surface showing the largest wall-normal extent of velocity deficit ($y \lesssim 0.6\delta$). This deficit increases with increasing modal content in the low-order representations and is largest for flow over the full surface. For example, the profile for the $M = 5$ model deviates least from the smooth-wall profile, indicating a reduced impact of roughness on the mean flow. In contrast, the mean profile for the $M = 16$ representation collapses quite well with the profile for the full surface, indicating that the 16 most dominant topographical modes (4.2% of the 383 total modes but 95% of the FSC) are sufficient for capturing the impact of the full surface on the mean velocity for developing flow.

4.1.2 Reynolds stresses

Figure 9(a) presents profiles of the streamwise and wall-normal Reynolds normal stresses, $\langle u'^2 \rangle$ and $\langle v'^2 \rangle$, normalized by U_e^2 for developing flow. Enhancement of the Reynolds normal stresses is evident with increasing modal content, with both $\langle u'^2 \rangle$ and $\langle v'^2 \rangle$ enhanced by roughly 40% in the full-surface case relative to smooth-wall flow. With regard to the low-order representations,
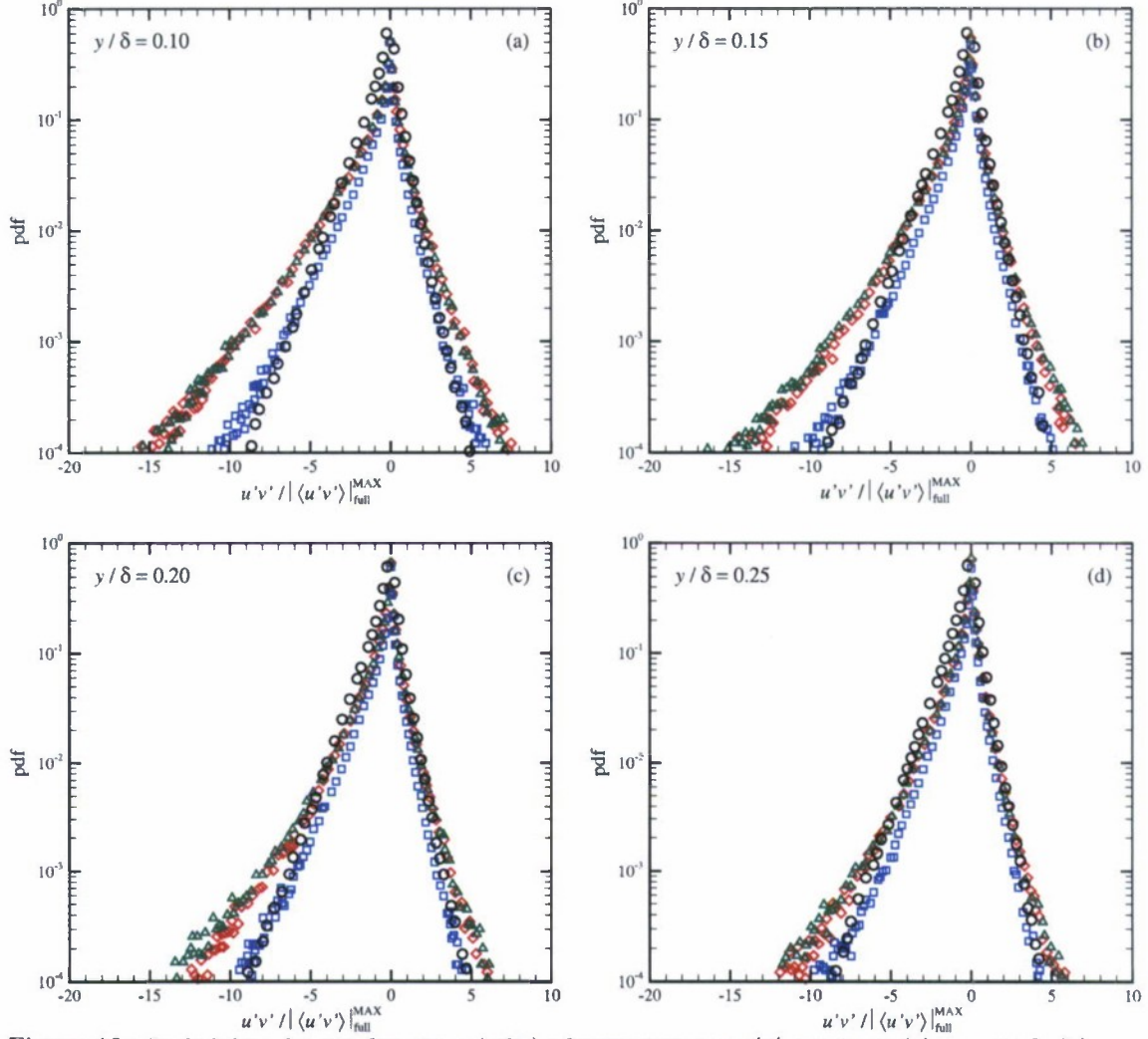
15

Figure 10: Probability density functions (pdfs) of instantaneous $u'v'$ events at (a) $y = 0.1\delta$, (b) $y = 0.15\delta$, (c) $y = 0.2\delta$ and (d) $y = 0.25\delta$ for developing flow. Not all data points shown for clarity. ◯: Smooth; ☐: $M = 5$ model; △: $M = 16$ model; ◇: Full surface.

the $M = 5$ model shows only moderate enhancement of $\langle v'^2 \rangle$ and $\langle u'^2 \rangle$ compared to the smooth-wall baseline. Consistent with the trends in the mean velocity, the $M = 16$ result shows strong consistency with the full-surface results except near $y = 0.1\delta$ where this low-order representation produces slightly lower values of $\langle u'^2 \rangle$ compared to the full surface. This observation highlights the importance of even finer-scale topographical details in the local flow behavior in the near-wall region. The wall-normal extent of the internal layer formed by the roughness grows with increasing modal content, with the internal layer for flow over the full surface and the $M = 16$ model extending to roughly $y \simeq 0.55\delta$ for both $\langle u'^2 \rangle$ and $\langle v'^2 \rangle$ but to only $y \simeq 0.4\delta$ for the $M = 5$ model. Beyond these wall-normal locations, the rough-wall profiles collapse well with smooth-wall flow.

Interestingly, the $M = 16$ model reproduces the full-surface mean RSS, $-\langle u'v' \rangle$, profile [figure 9(b)] extremely well over the entire wall-normal range over which measurements were possible, including replication of the wall-normal extent of the internal layer for the full surface ($y \simeq 0.5\delta$). This measure of the internal-layer thickness for both the $M = 16$ model and the full surface is slightly smaller than that noted from the mean velocity and Reynolds normal stress profiles. In contrast, the $M = 5$ model yields much lower values of mean RSS as well as a thinner internal layer ($y \simeq 0.35\delta$), though the magnitude of the $M = 5$ mean RSS is still larger than
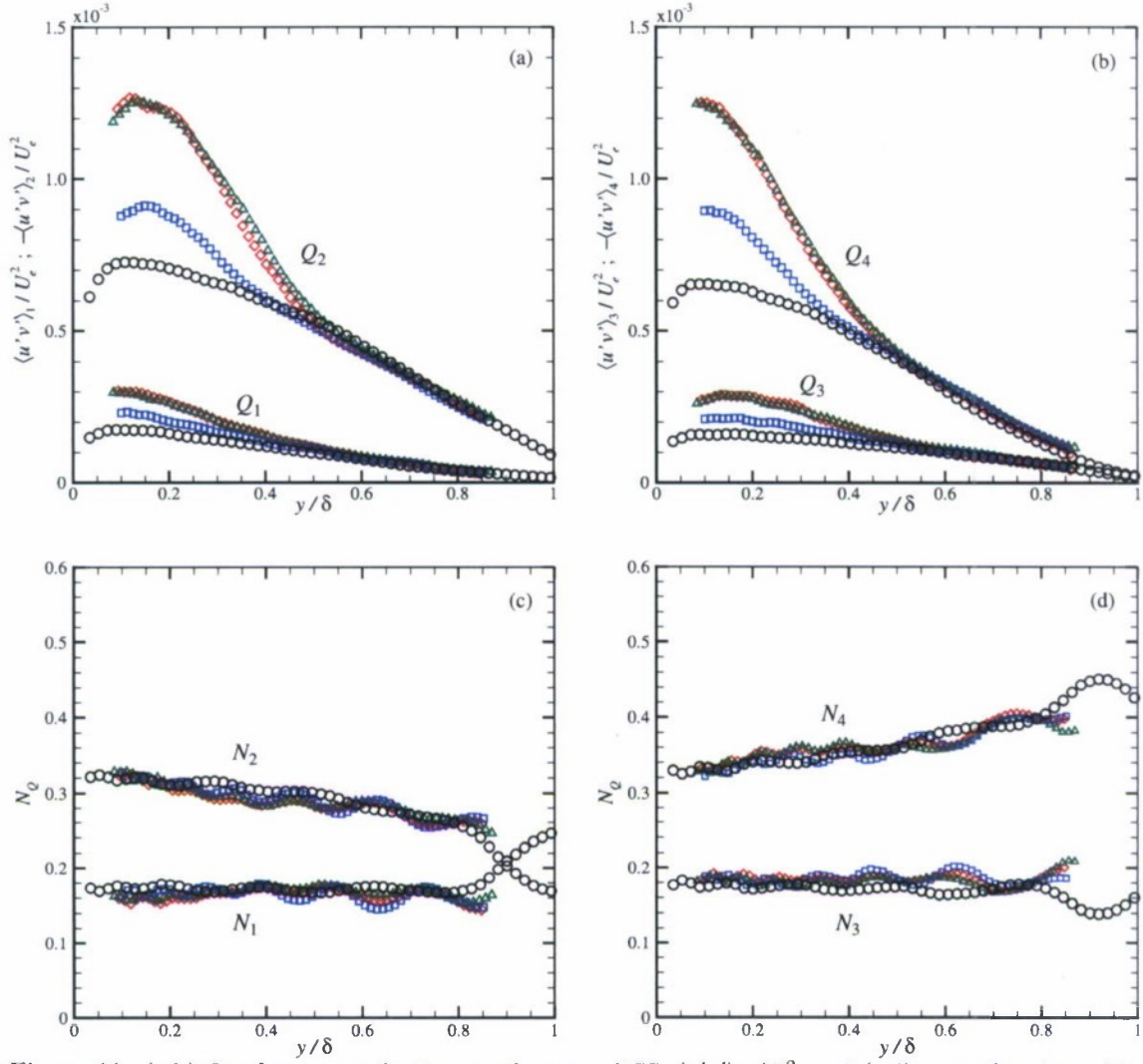
16

Figure 11: (a,b) Quadrant contributions to the mean RSS, $\langle u'v'\rangle_Q/U_e^2$, and (c,d) space fractions, N_Q, for developing flow as a function of wall-normal position for $H = 0$. Not all data points shown for clarity. $\bigcirc$: Smooth; $\square$: $M = 5$ model; $\triangle$: $M = 16$ model; $\diamond$: Full surface.

that for the smooth wall. To further explore these trends, particularly the contributions of the various events that yield the overall mean RSS (ejections, sweeps, inward/outward interactions), figure 10 presents pdfs of instantaneous $u'v'$ events at various wall-normal locations for flow over all surface cases. Event magnitudes are normalized by the magnitude of the peak mean RSS for the full-surface case in order to directly compare the efficacy of the low-order surface models in reproducing the flow behavior of the full surface. Consistent with the trends noted in the mean RSS profiles, the $M = 5$ model does not reproduce the pdf of the full surface, most notably close to the wall. These differences are apparent in both the negative and positive tails of the pdfs, meaning that all four quadrant events are likely modified in the $M = 5$ model compared to the full surface. In contrast, the $M = 16$ surface model produces pdfs that are quite consistent with the character of their full-surface counterparts. Far from the wall, the pdfs from all three surfaces collapse toward the smooth-wall trends as the outer-edge of the internal roughness layer is approached.
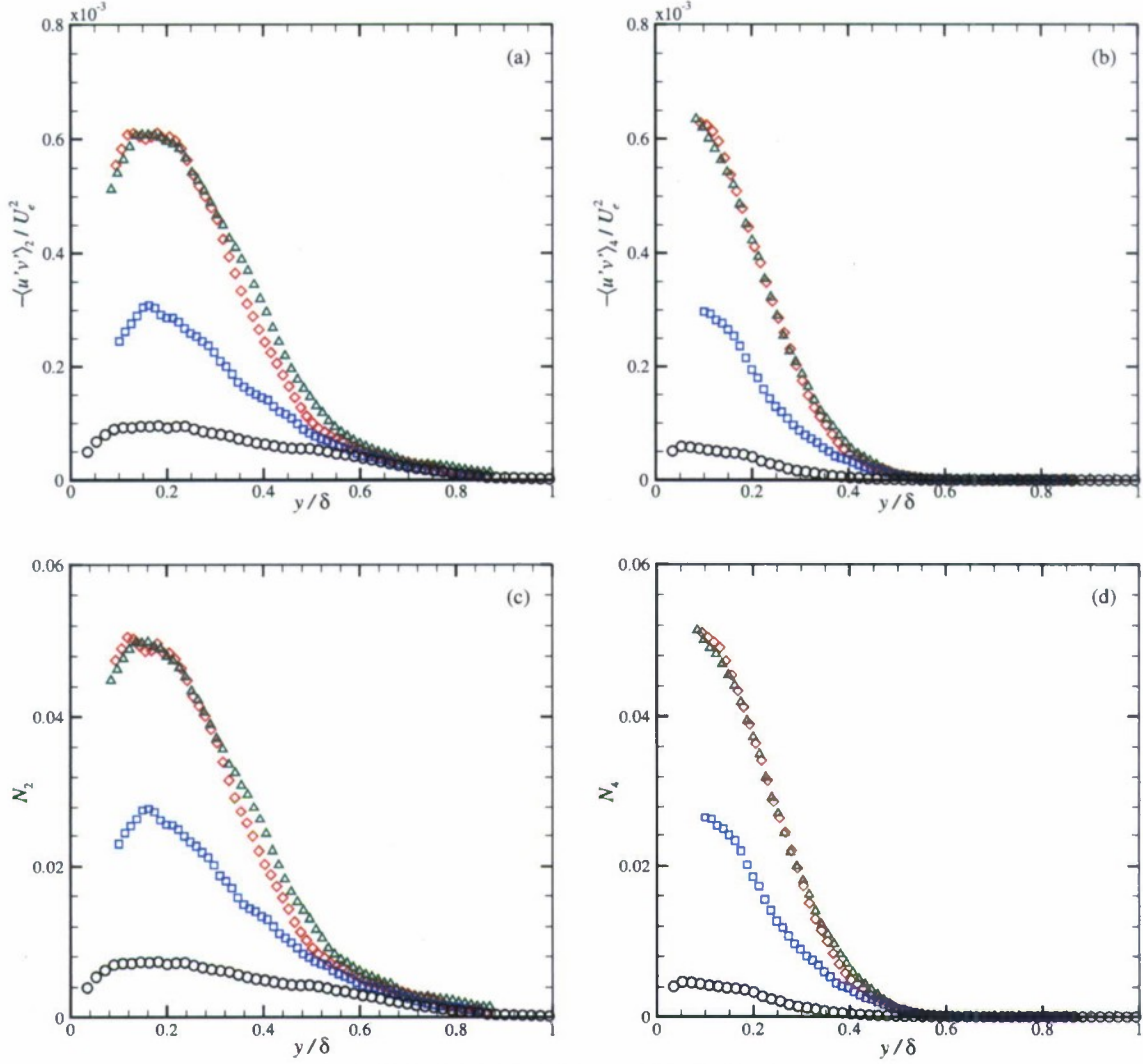
Figure 12: As in figure 11 but $H = 4$.

4.1.3 Quadrant analysis

Extending the analysis afforded by pdfs of instantaneous RSS-producing events, quadrant analysis is employed to assess how consistent the various quadrant contributions to the mean RSS profiles are amongst all surface conditions. Figures 11(a) and 11(b) present contributions of the four quadrant events to the mean RSS for a threshold of $H = 0$ wherein all instantaneous $u'v'$ events are included in the decomposition. Consistent with the mean RSS profiles, ejections (Q_2) and sweeps (Q_4) dominate over inward (Q_4) and outward (Q_1) interactions for all cases. Of particular interest, while the $M = 5$ model fails to reproduce the quadrant contributions of the full-surface flow, all four quadrant contributions to the mean RSS for the $M = 16$ low-order representation are quite consistent with those for the full surface. Outside the internal layer generated by roughness ($y \simeq 0.4\delta$ and 0.5δ for the $M = 5$ model and the $M = 16$ model/full surface, respectively), the quadrant contributions collapse well with the smooth-wall results. In contrast to the roughness-induced enhancement noted in the quadrant contributions to the mean RSS, the space fractions of these quadrant events are found to be similar for all surface cases [figures 11(e) and 11(d)]. Thus, roughness does not appear to produce more numerous RSS-producing events but instead tends to intensify the magnitude of these events compared to smooth-wall flow for $H = 0$.

Surface	Re_θ	U_e (m/s)	δ (mm)	u_τ (m/s)	y_* (μm)	δ^+	ΔU^+	k^+	k_s^+	$5k/\delta$
Full surface	14 340	17.25	101.9	0.785	19.5	5 215	8.2	218	107	0.21
$M = 16$ model	13 300	17.2	98.6	0.785	19.8	4 950	7.9	207	95	0.21
$M = 5$ model	12 590	17.3	96.6	0.723	21.1	4 580	5.7	173	–	0.19

Table 3: Relevant experimental parameters for developed-flow experiments.

Figures 12(a) and 12(b) present quadrant contributions for the three rough surfaces and the smooth-wall baseline for a threshold defined by $H = 4$ which allows only the most intense $u'v'$ events to be included in the decomposition. Note that only ejections (Q_2) and sweeps (Q_4) are presented since the contributions of inward and outward interactions are near zero for this threshold. Consistent with the $H = 0$ trends, the $M = 16$ surface model reproduces the full-surface trends quite well while the $M = 5$ model does not. Of interest, while the space fractions for the $H = 0$ threshold showed little difference in the number of quadrant events generated by the two low-order models compared to the full-surface and smooth-wall flow, the space fractions for $H = 4$ [figures 12(c) and 12(d)], which includes only the most intense RSS-producing events, show clear differences from smooth-wall flow. In particular, the $M = 16$ model reproduces the space fractions of both ejections and sweeps from the full-surface flow quite well. In contrast, the $M = 5$ model fails to reproduce the quantitative behavior of the full-surface flow. Nevertheless, compared to smooth-wall flow, all of the rough-wall cases are found to generate more numerous intense ejection and sweep events by a factor of 3–6. Finally, outside the internal layer the rough-wall quadrant contributions and associated space fractions again collapse well with the smooth-wall results as should be expected for developing flow.

4.2 Developed Flow

This section presents results from the PIV measurements made $\sim 25\delta$ downstream of the leading edge of the roughness such that the rough-wall flows have attained self-similar states based on past measurements over such surfaces [26]. Table 3 summarizes relevant experiment parameters for these developed-flow measurements.

4.2.1 Mean velocity

Figure 13 presents mean velocity profiles for flow over the two low-order models, the full surface and the smooth-wall baseline in both inner units (normalized by u_τ and ν) and in velocity defect form (normalized by u_τ and δ). The friction velocity, u_τ, for each case was determined using the total shear stress method which assumes a region of constant shear stress equal to the wall shear stress in the overlap and inner region of the boundary layer [19, 26]. These values of u_τ were then used to determine the virtual origin, $y_\circ$, and the roughness function, ΔU^+, for the rough-wall cases by fitting the mean velocity profile to the expected logarithmic profile in the log layer given by

$$U^+ = \frac{1}{\kappa} \ln(y^+ - y_\circ^+) + A - \Delta U^+, \tag{13}$$

where $\kappa = 0.41$ and $A = 5.3$ are the log-law constants. Knowledge of ΔU^+ enables one to relate the roughness studied herein to the sand-grain experiments of Nikuradse[4] via an equivalent sand-grain height, k_s^+, that yields the same ΔU^+ as the present rough surfaces through the fully-rough asymptote given by

$$\Delta U^+ = \frac{1}{\kappa} \ln(k_s^+) + A - 8.5. \tag{14}$$

It should be noted that the constant stress method for determining u_τ has an uncertainty of approximately 4–6% [19, 18] so the symbol size of the statistics presented in this section reflect
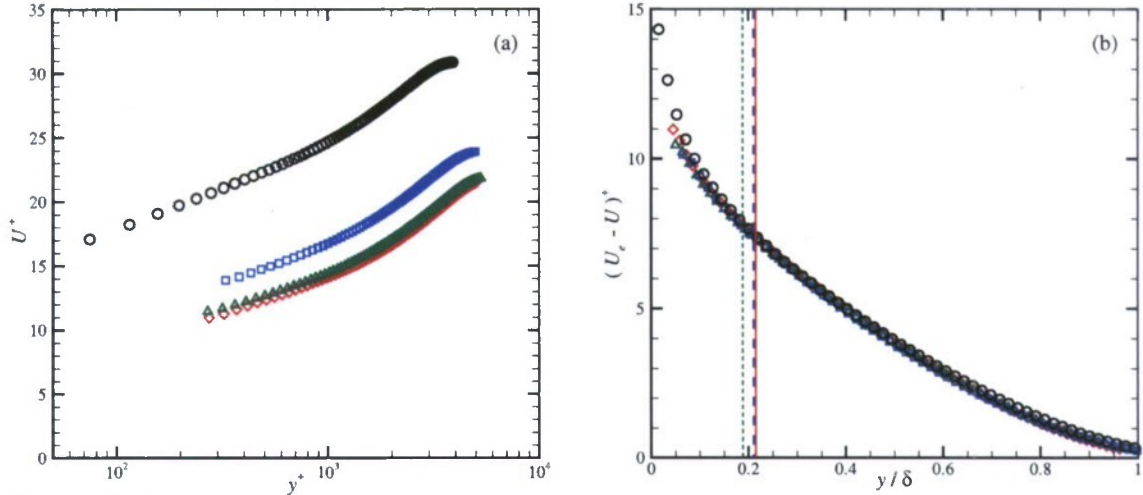
Figure 13: Mean velocity profiles in (a) inner units and (b) velocity defect form for developed flow. Solid, dashed and dotted lines in (b) demarcate the $5k/\delta$ positions for the full, $M = 16$ and $M = 5$ cases, respectively, and not all data points shown for clarity. $\bigcirc$: Smooth; $\square$: $M = 5$ model; $\triangle$: $M = 16$ model; $\diamond$: Full surface.

this uncertainty bound.

The inner-scaled profiles [figure 13(a)] reveal the downward shift of the rough-wall profiles relative to the smooth-wall profile due to the increased skin friction at the wall. Of interest, while the inner-scaled mean profile for the $M = 5$ case resides between the smooth and full-surface profiles ($\Delta U^+ = 5.7$ for the $M = 5$ model), the $M = 16$ case ($\Delta U^+ = 7.9$) sits just above, but nearly reproduces, the full-surface profile ($\Delta U^+ = 8.2$). One can therefore infer that the largest topographical scales of the full surface dominate ΔU^+ for the roughness considered herein, though a slight difference does exist which could represent contributions of excluded topographical modes to ΔU^+. However, this possibility cannot be confirmed as the difference between the 16-mode and full-surface ΔU^+ is within the uncertainty in determining this quantity (3–5%). In contrast, the mean velocity profiles in defect form [figure 13(b)] show strong consistency between all surface cases outside the roughness sublayer ($y \gtrsim 0.2\delta$), consistent with Townsend's wall similarity hypothesis, and also confirm the attainment of a self-similar state for all cases. Within the roughness sublayer, all three roughness cases sit below the smooth-wall case (consistent with many past studies of both idealized [13, 14, 15, 19] and realistic roughness [25, 26]) yet both low-order representations reproduce the full-surface profile well.

4.2.2 Reynolds stresses

Figure 14 presents profiles of $\langle u'^2 \rangle^+$, $\langle v'^2 \rangle^+$ and $-\langle u'v' \rangle^+$ for all surface cases. Consistent with Townsend's wall similarity hypothesis, the smooth, full-surface and model profiles collapse outside the roughness sublayer ($y \gtrsim 0.2\delta \cong 5k$). However, some differences are noted within the roughness sublayer. In the case of $\langle u'^2 \rangle^+$ [figure 14(a)], all three rough-wall cases sit below the smooth-wall profile which is a well-known effect of roughness in wall turbulence. However, while the $M = 5$ and $M = 16$ cases collapse with one-another, they both yield slightly lower values of $\langle u'^2 \rangle^+$ compared to the full surface. This discrepancy is not entirely unexpected since the details of the roughness can have a significant impact on the local flow behavior close to the surface. As such, the higher-order topographical modes missing in the model surfaces appear to play a measurable role in $\langle u'^2 \rangle^+$ within the roughness sublayer. With regard to $\langle v'^2 \rangle^+$ [figure 14(a)], much better consistency is noted as both the 5- and 16-mode models reproduce the full-surface behavior well, even in the roughness sublayer. In contrast, both low-order surface
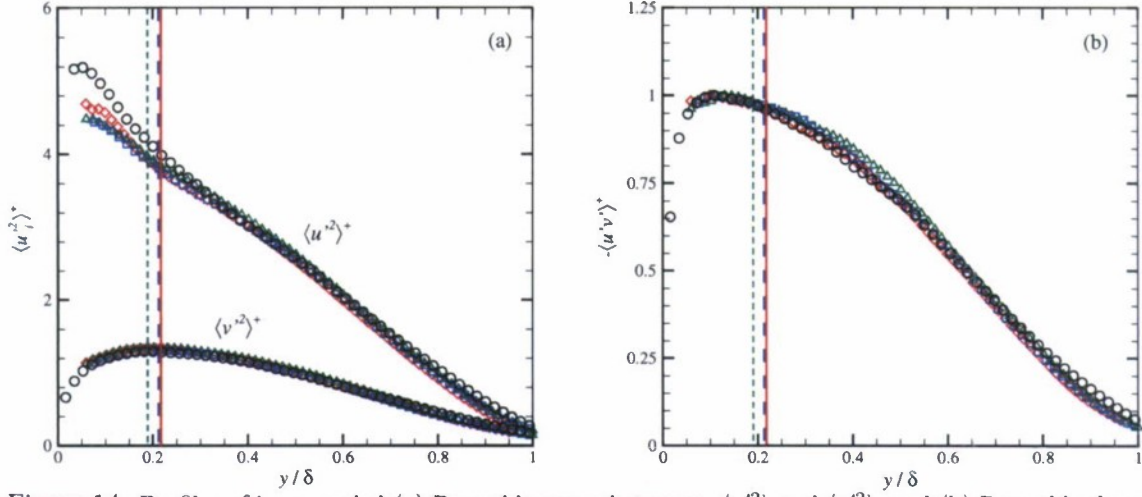
20

Figure 14: Profiles of inner-scaled (a) Reynolds normal stresses, $\langle u'^2 \rangle$ and $\langle v'^2 \rangle$, and (b) Reynolds shear stress, $-\langle u'v' \rangle$, for developed flow. Lines as in figure 13(b) and not all data points shown for clarity. ○: Smooth; □: $M = 5$ model; △: $M = 16$ model; ◇: Full surface.

models generate mean RSS profiles [figure 14(b)] that mimic the overall full-surface behavior well even within the roughness sublayer.

While the mean RSS profiles for the low-order surface models seem to reproduce the mean RSS behavior of flow over the full surface, this collapse need not require that the distributions of the instantaneous $u'v'$ events contributing to these mean profiles be identical for flow over the full surface and the two low-order models. To explore such issues, figure 15 presents pdfs of instantaneous $u'v'$ events contributing to the mean RSS profiles at $y/\delta = 0.1$, 0.15, 0.2 and 0.3 computed for all surface cases. While the pdfs of $u'v'$ events away from the wall [figures 15(d)] show strong similarity regardless of surface condition, the pdfs of $u'v'$ events within the roughness sublayer [figures 15(a)–(c)] indicate that flow over both the $M = 5$ and $M = 16$ surface models do not reproduce the number of intense and negative $u'v'$ events observed for flow over the full surface. As such, the low-order surface models appear to produce slightly fewer extremely intense ejection and/or sweep events compared to the full surface. In contrast, the positive tails of the pdfs in figure 15 show better collapse, even in the roughness sublayer, indicating that these positive contributions to $\langle u'v' \rangle^+$ are less affected by the finer-scale details of the surface topography.

4.2.3 Quadrant analysis

To study these trends in RSS-producing events further, quadrant analysis is employed to distinguish ejection from sweep contributions and inward- from outward-interaction contributions to the mean RSS profile for all surface cases. Figures 16(a) and 16(b) present quadrant contributions for a threshold given by $H = 0$, meaning that all contributions, weak through intense, are included in the decomposition. As should be expected from the behavior of the mean RSS profiles [figure 14(b)] and the pdfs of $u'v'$ events (figure 15), Q_2 and Q_4 contributions dominate over Q_1 and Q_3 contributions. In particular, the profiles of Q_2 and Q_4 contributions are consistently 3–4 times larger in magnitude than those of Q_1 and Q_3 events. Further, the rough-wall results show strong consistency with the smooth-wall baseline outside the roughness sublayer, again consistent with Townsend's hypothesis. With regard to the consistency between the profiles of the low-order models and those of the full surface, while the Q_1, Q_3 and Q_4 profiles collapse regardless of surface, the contributions of ejections (Q_2) show surface dependence close to the wall with both surface models yielding slightly weaker contributions of ejections to the mean RSS for the case of $H = 0$. This behavior is consistent with the surface-dependent
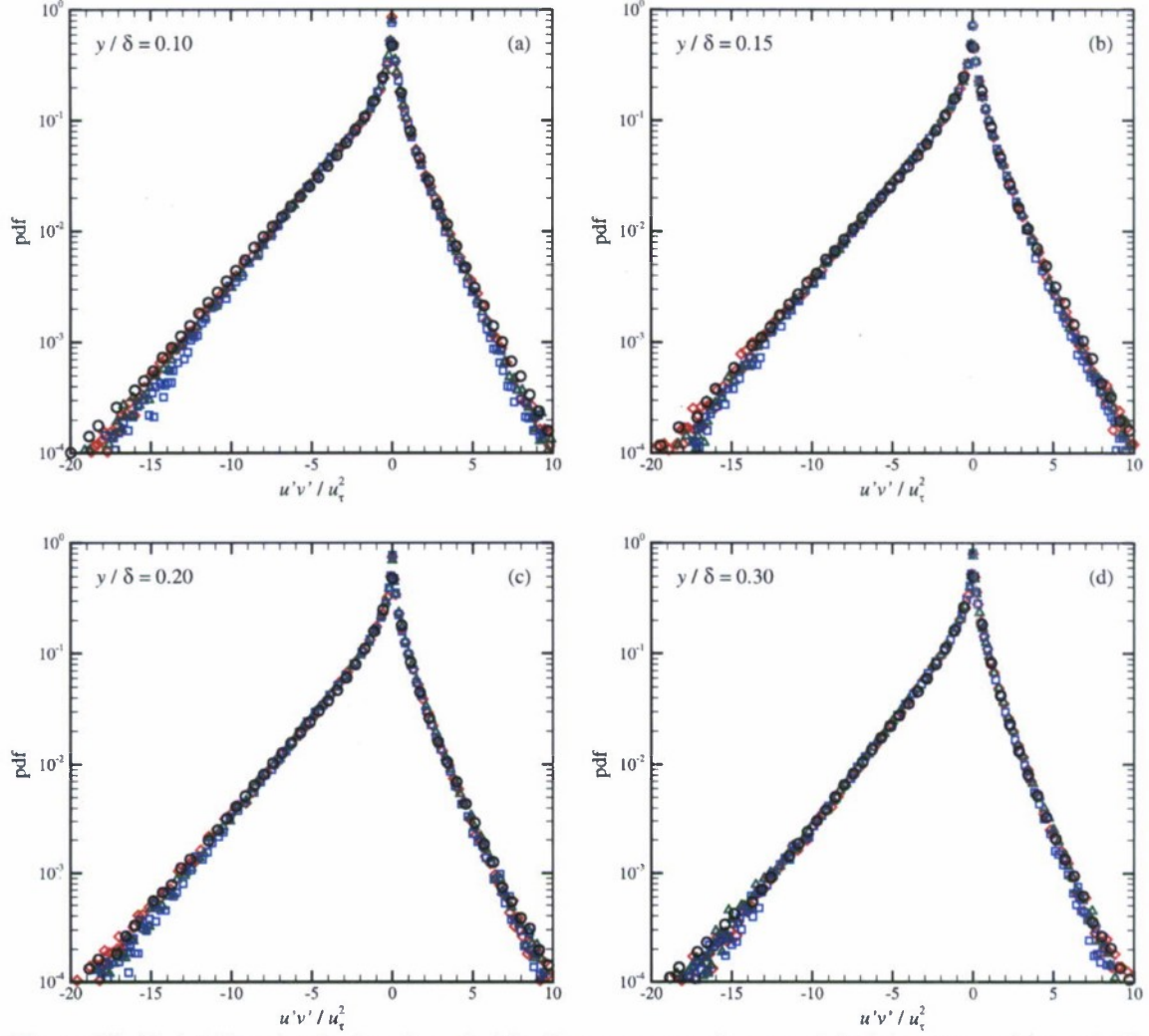
Figure 15: Probability density functions (pdfs) of instantaneous inner-scaled $u'v'$ events at (a) $y = 0.1\delta$, (b) $y = 0.15\delta$, (c) $y = 0.2\delta$ and (d) $y = 0.3\delta$ for developed flow. Not all data points shown for clarity. $\bigcirc$: Smooth; $\square$: $M = 5$ model; $\triangle$: $M = 16$ model; $\Diamond$: Full surface.

behavior noted in the pdfs of $u'v'$ events where the full surface was found to produce slightly more numerous intense negative $u'v'$ events than the two low-order surface models. As such, this observation may indicate that it is more numerous ejection events in the full-surface case that are primarily responsible for the surface-dependent behavior noted in the pdfs of figure 15 within the roughness sublayer. Despite this difference, the fraction of space, N_Q, occupied by these various events [figures 16(a) and 16(b)] are quite similar for the different surface cases except near the boundary-layer edge where the weak magnitude of the velocity fluctuations can introduce increased uncertainty in quadrant decomposition.

Figure 17 presents quadrant contributions and space fractions for a threshold of $H = 4$, meaning that only the contributions of the most intense $u'v'$ events to the mean RSS are considered. While the $M = 5$ and $M = 16$ surface models clearly yield weaker contributions of intense Q_2 events compared to the full-surface case (larger discrepancy but still qualitatively consistent with the $H = 0$ trends), these surfaces actually generate slightly higher contributions from Q_4 events compared to the full-surface result. As such, the finer-scale topographical details of the full surface excluded from the low-order surface models may actually contribute in a meaningful way to the generation of intense Q_2 and Q_4 events. Despite these near-wall differences, good consistency is noted between the smooth- and rough-wall results outside the
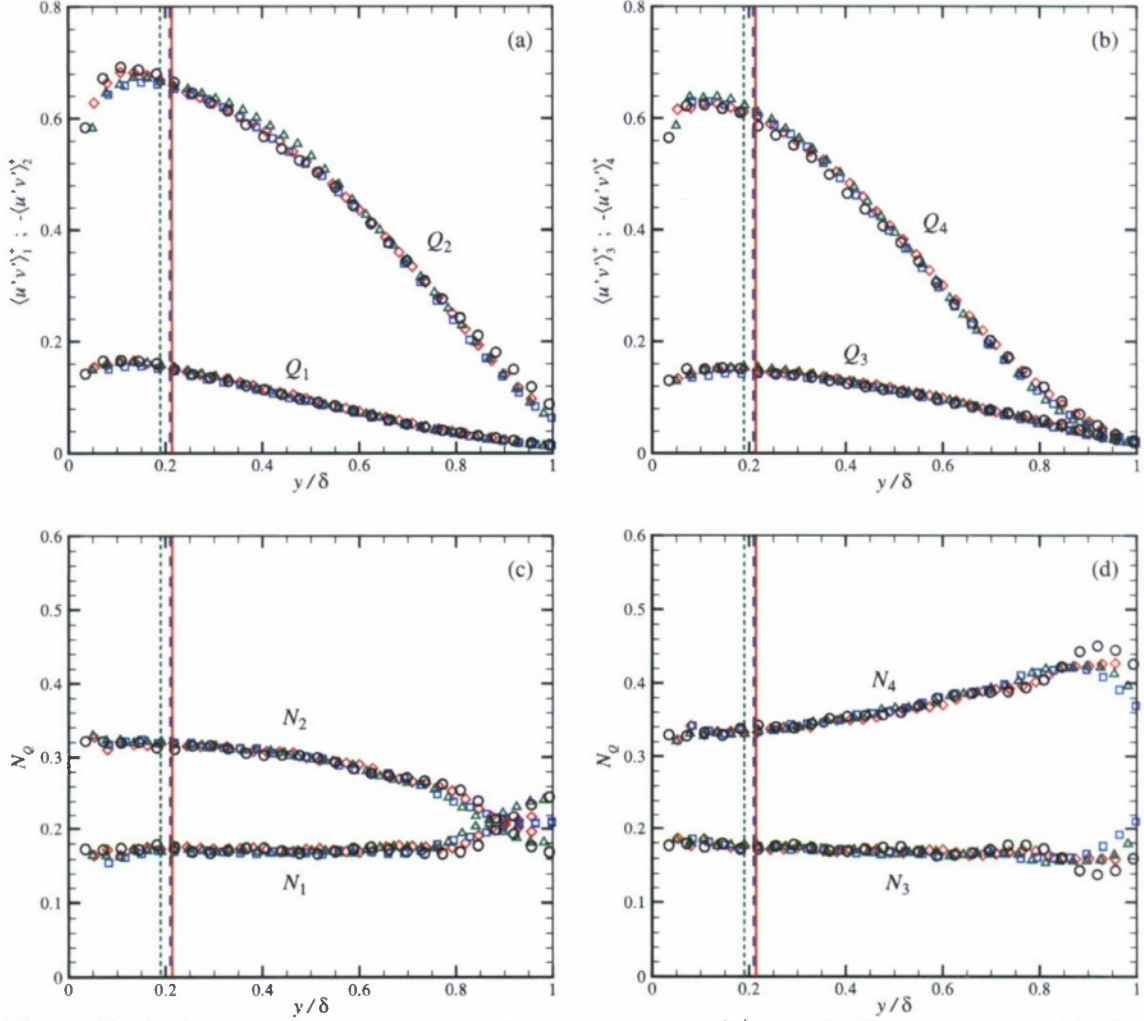
Figure 16: (a,b) Quadrant contributions to the mean RSS, $\langle u'v' \rangle_Q^+$, and (c,d) space fractions, N_Q, for developed flow as a function of wall-normal position for $H = 0$. Lines as in figure 13(b) and not all data points shown for clarity. $\bigcirc$: Smooth; $\square$: $M = 5$ model; $\triangle$: $M = 16$ model; $\Diamond$: Full surface.

roughness sublayer in accordance with outer-layer similarity.

4.2.4   Two-point velocity correlations

Figure 18 presents two-point correlation coefficients of streamwise velocity, ρ_{uu}, at $y/\delta = 0.1$, 0.15, 0.2 and 0.3 for flow over all surface conditions. While the correlations are computed within the two-dimensional measurement plane, they are presented in one-dimensional form herein to quantitatively assess their dependence on streamwise separation, Δx. Well within the roughness sublayer at $y = 0.1\delta$ [figure 18(a)], while the correlations at small Δx collapse irrespective of surface condition, there exists a shortening in the streamwise extent of ρ_{uu} at larger Δx for the three rough-wall cases is evident compared to the smooth-wall baseline. These trends indicate that the larger spatial scales of the flow are more sensitive to roughness effects than are the smaller scales of the flow. Interestingly, the two low-order representations produce a slightly more pronounced streamwise shortening of ρ_{uu} than the full surface. With increasing distance from the wall this difference between the full-surface and low-order-representation profiles diminishes quickly as the two low-order models collapse well with the full-surface result at $y = 0.15\delta$ [figure 18(b)] and $y = 0.2\delta$ [figure 18(c)], though all three rough-wall results still show shortening compared to the smooth-wall baseline. Outside the roughness sublayer at
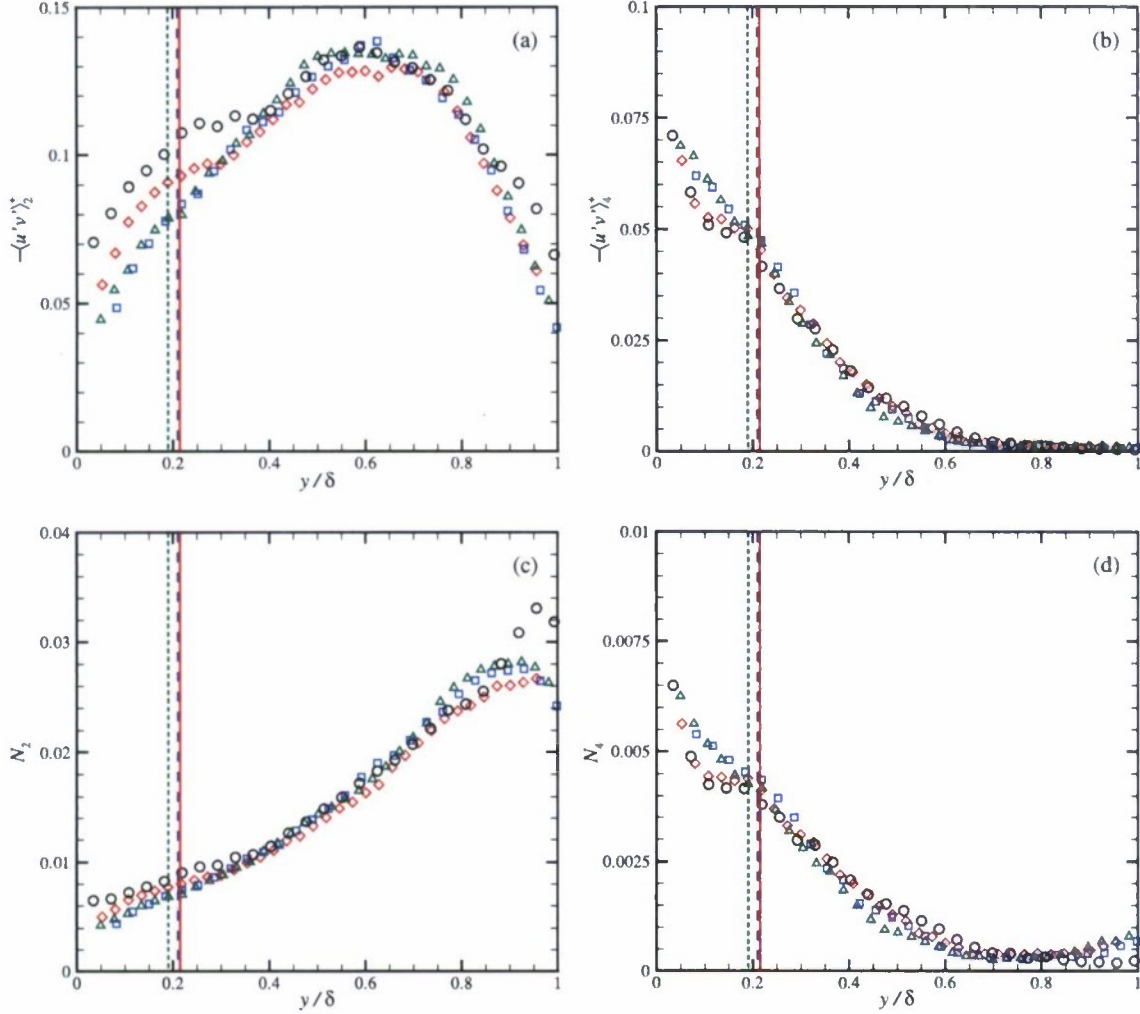
23

Figure 17: As in figure 16 but $H = 4$.

$y = 0.3\delta$ [figure 18(d)], however, the rough-wall correlations collapse well with the smooth-wall result which is consistent with Townsend's wall similarity hypothesis. This collapse therefore suggests similarity in the average spatial structure of the smooth-wall flow with that of the rough-wall flows.

The two-point correlation coefficient of wall-normal velocity, ρ_{vv}, presented in figure 19 shows less influence of roughness, though a slight broadening of ρ_{vv} is noted close to the wall at $y = 0.1\delta$ [figure 19(a)] and $y = 0.15\delta$ [figure 19(b)] for the three rough-wall cases compared to the smooth-wall baseline. However, in contrast to the trends noted at these wall-normal locations for ρ_{uu}, the low-order representations yield ρ_{vv} profiles that match that of the full-surface flow very well. With increasing distance from the wall, ρ_{vv} is found to collapse irrespective of surface condition. Comparing the streamwise extent of ρ_{vv} to that of ρ_{uu}, it is clear that the latter is more representative of the larger spatial scales of the flow while the former is more strongly influenced by the smaller spatial scales. Finally, figure 20 presents streamwise profiles of the cross-correlation coefficient of the streamwise and wall-normal velocities, ρ_{uv}. Similar to ρ_{vv}, the streamwise extent of ρ_{uv} is enhanced within the roughness sublayer at $y = 0.1\delta$ and 0.15δ (figures 20(a) and 20(b), respectively) compared to smooth-wall flow, though the profiles for the low-order representations collapse well with the full-surface results. With increasing wall-normal position [figures 20(c) and 20(d)] these differences between the smooth- and rough-wall cases diminish indicating little impact of roughness on the average spatial structure embodied
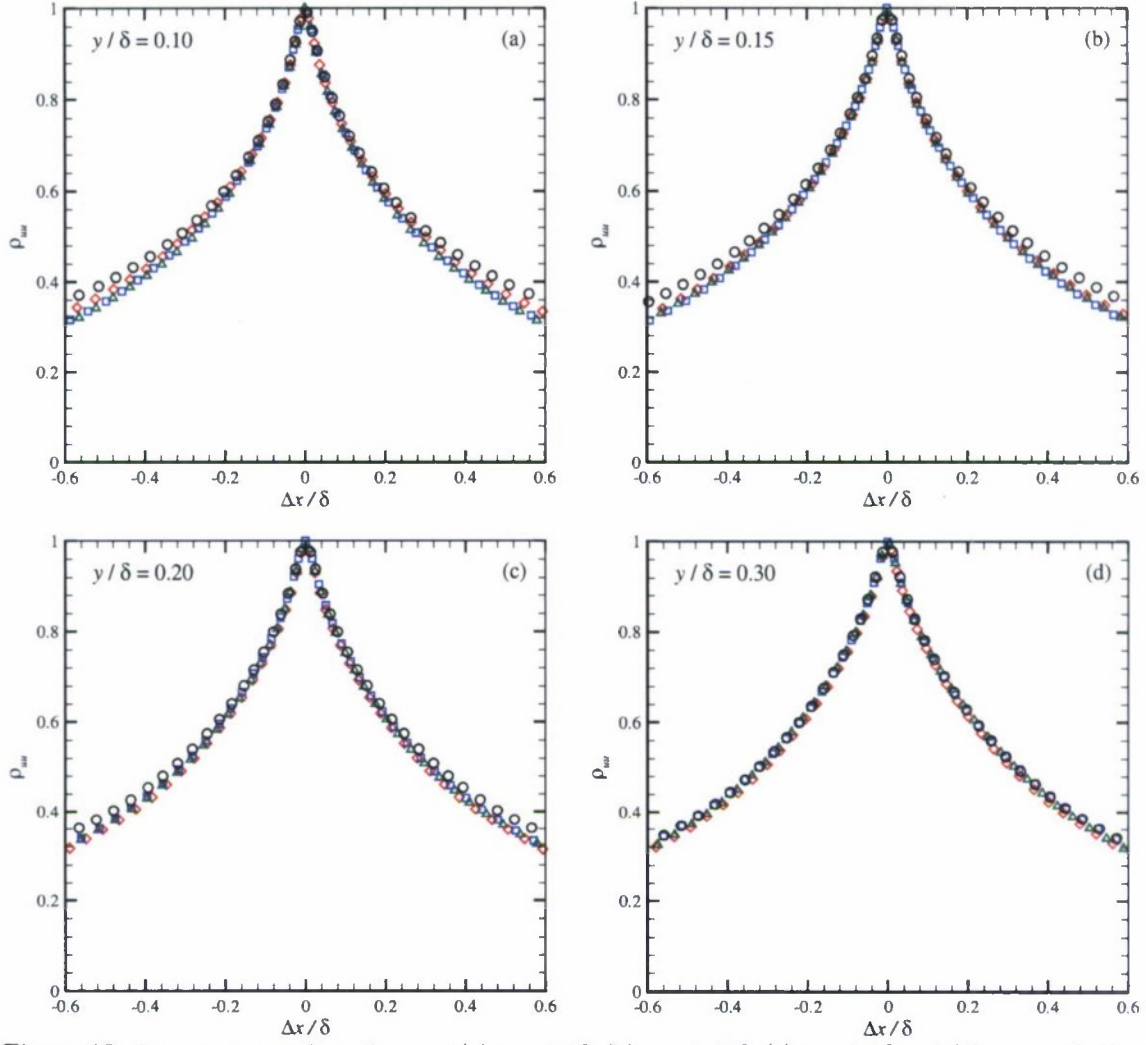
24

Figure 18: Streamwise profiles of ρ_{uu} at (a) $y = 0.1\delta$, (b) $y = 0.15\delta$, (c) $y = 0.2\delta$ and (d) $y = 0.3\delta$. Not all data points shown for clarity. ○: Smooth; □: $M = 5$ model; △: $M = 16$ model; ◇: Full surface.

in ρ_{uv} outside the roughness sublayer.

5 Streamwise–Spanwise Plane Measurements at $y = 0.047\delta$

Given the observations discussed above, particularly the notable differences observed between flow over the low-order models and the full surface in the roughness sublayer, wall-parallel stereo PIV measurements were performed at $y = 0.047\delta$ for all three rough surfaces ($y = 0$ in the rough-wall cases is positioned at the virtual origin determined from the modified Clauser chart analysis) as well as the smooth-wall baseline to explore these differences further. Figure 21 presents contour maps of the roughness topographies directly beneath the $x - z$ measurement planes for each surface so that the local topographical characteristics can be contrasted with the data to be presented.

Figures 22–28 present contour plots of various single-point statistics for all four surface cases with green contours in the background highlighting the roughness patterns beneath the measurement plane. However, before discussing the details of these fields, table 4 presents the area-averaged values of the streamwise velocity defect as well as the streamwise and wall-normal Reynolds normal stresses and the RSS. These values are close, but not identical, to their
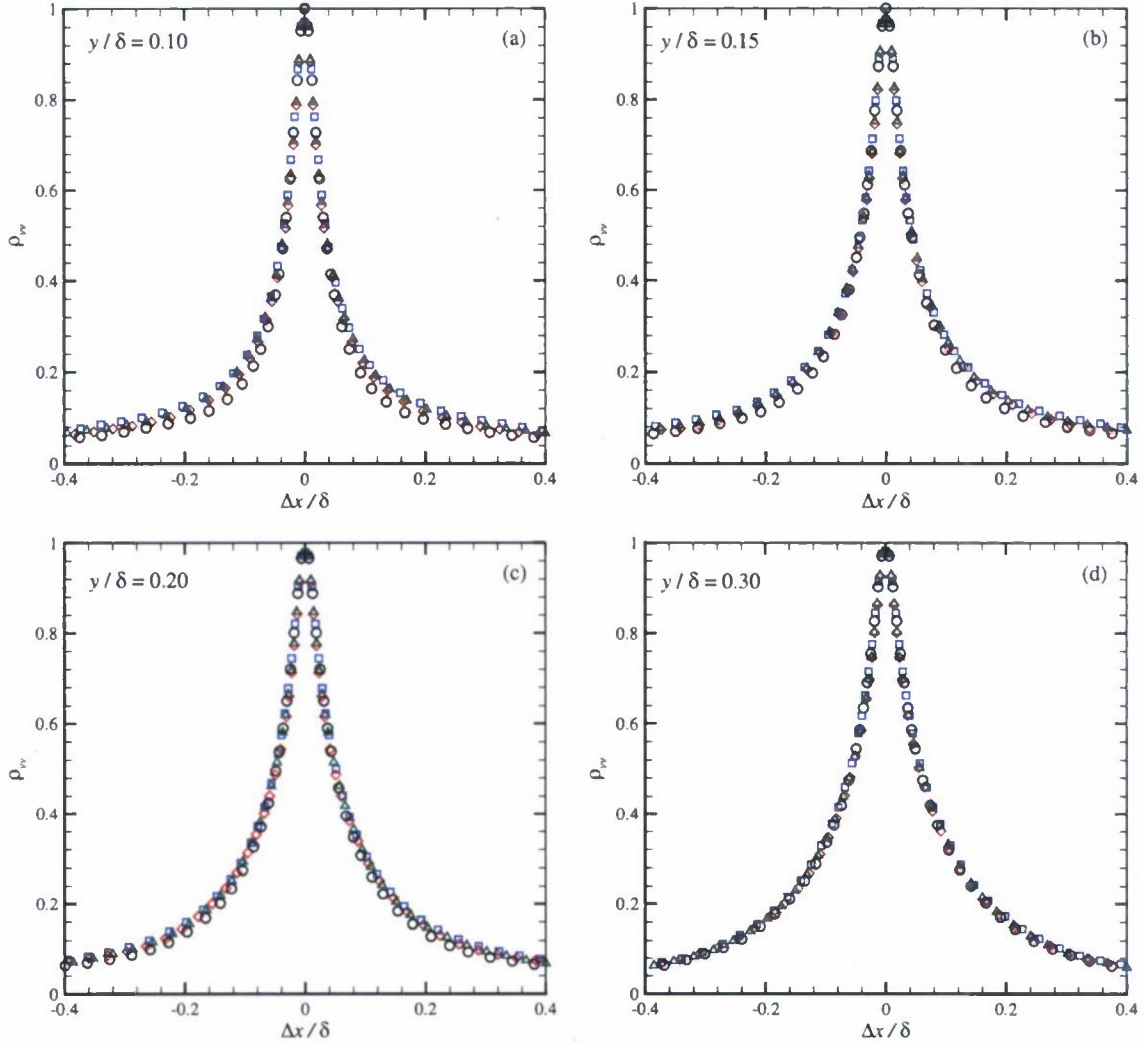
Figure 19: As in figure 18 but ρ_{vv}.

counterparts from the $x - y$ experiments shown in figures 13 and 14. These small differences can be explained by recalling that the $x - y$ measurements were performed at a single spanwise location (demarcated in figure 21 by the dashed lines) while the values presented in figure 4 were averaged over an area spanning many different topographical details in the spanwise direction. Thus, the local details of the topography can lead to slight differences in the values of the single-point statistics.

5.1 Mean velocity

Prior to discussing the details of the ensemble-averaged turbulence statistics, it should be noted that the smooth-wall results are presented as a baseline for comparison as these statistics should be nearly homogeneous across the δ-scale field of view. Thus, any variability noted in these statistics represents a measure of their sampling error. Therefore, any spatial variability observed in the rough-wall statistics can be compared to the variability in the smooth-wall baseline as a means of discerning whether it is due to roughness effects or simply an artifact of sampling. The ensemble average of streamwise velocity in defect scaling, $\langle U_e - u \rangle^+$, is shown in figure 22 for the smooth-wall base line as well as the three rough-wall cases ($M = 5$, $M = 16$ and full surface). While the smooth-wall result is quite uniform, all rough-wall flows exhibit
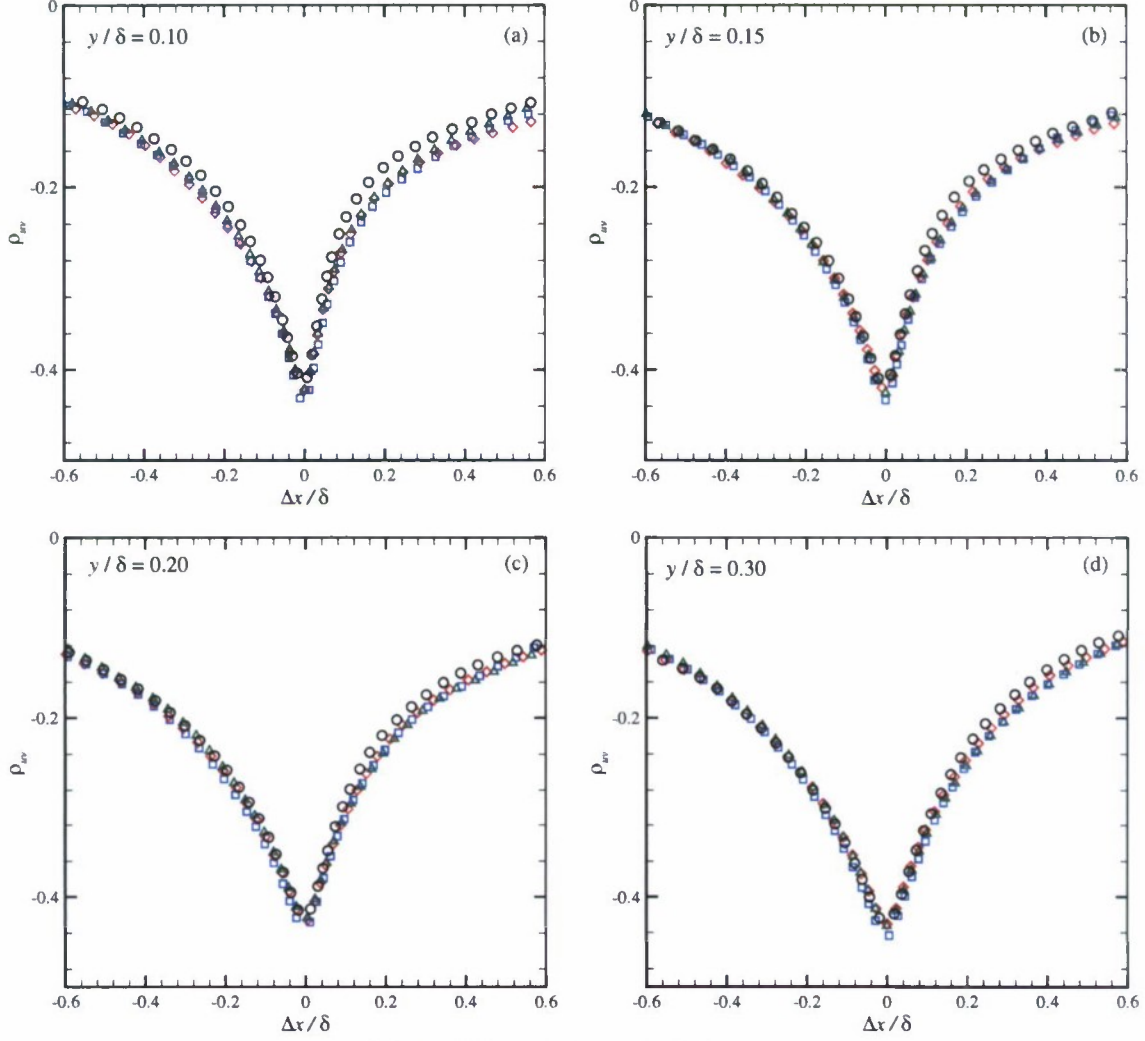
Figure 20: As in figure 18 but ρ_{uv}.

a spanwise-localized low-momentum region, bounded by high-momentum regions. This result suggests that the roughness under consideration induces a "channeling" effect in the flow. This low-momentum region is located near $z \approx 0.3\delta$ for the $M = 5$ case [figure 22(b)], while the $M = 16$ and full-surface cases show a low-momentum region near $z \approx 0.5\delta$ [figures 22(c) and 22(d), respectively]. Further, it is observed that the peak values of the low- and high-momentum regions are higher in the $M = 5$ model than in the other two rough-wall cases.

The ensemble-averaged wall-normal velocity, $\langle v \rangle^+$, is shown in figure 23. The smooth-wall result [figure 23(a)] is nearly zero across the field of view, as one would expect. However, while the streamwise velocity defect showed larger-scale influences of the roughness, $\langle v \rangle^+$ exhibits more localized influences of the roughness. In particular, $\langle v \rangle^+$ is positive just upstream of a large-scale peak in roughness and negative just downstream of such a surface feature. Thus, as one might expect, the flow is diverted away and toward the wall by the roughness features that occur directly beneath the measurement plane. These vertical excursions of the flow toward and away from the wall are strongest for the $M = 5$ case [figure 23(b)] which only embodies the largest topographical scales of the full surface. Of interest, the $M = 16$ result [figure 23(c)] is remarkably consistent with the full-surface result [figure 23(d)], indicating that the intermediate topographical scales embodied in modes 6–16 that are missing in the $M = 5$ model play an important role in this mean vertical motion of the flow. As mentioned earlier, these intermediate
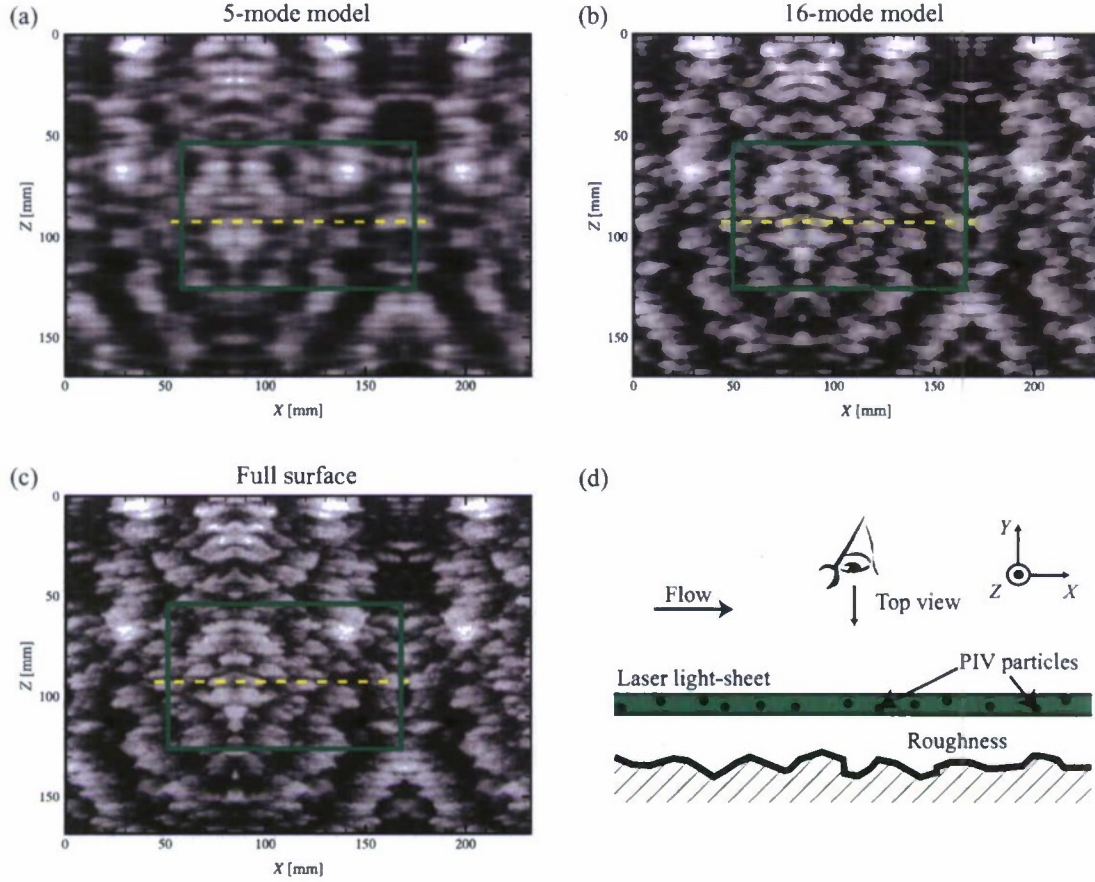
27

Figure 21: Local roughness topography below the $y = 0.047\delta$ wall-parallel fields of view (demarcated by boxed regions) for the (a) $M = 5$ model, (b) $M = 16$ model and (c) full surface. The dashed lines represent the position of the $x - y$ PIV measurements. (d) Schematic illustrating stereo PIV view of the flow in the wall-parallel field of view above the surfaces.

topographical scales add to the jagged and irregular character of the largest roughness elements present in the topography.

5.2 Reynolds stresses

The results for ensemble-averaged streamwise Reynolds normal stress, $\langle u'^2 \rangle^+$, are presented in figure 24. As with the mean velocity components, the smooth-wall baseline [figure 24(a)] shows only slight variability across the field of view ($\sim 10\%$) which is a measure of the sampling error in this second-order statistic. The rough-wall results, however, show significant variability. Of particular interest, the $M = 16$ and full-surface results [figures 24(c) and 24(d), respectively] display distinct streamwise-elongated regions of intense $\langle u'^2 \rangle^+$ (one at $z \approx 0.35\delta$ and the other at $z \approx 0.65\delta$) between which a region of slightly weaker $\langle u'^2 \rangle^+$ is noted. This elongated region of weaker $\langle u'^2 \rangle^+$ is coincident with the low-momentum region noted in the $M = 16$ and full-surface streamwise velocity defect results (figure 22) while the elongated regions of intense $\langle u'^2 \rangle^+$ are coincident with the spanwise boundaries of the low-momentum region. A similar pattern is also notable in the $M = 5$ $\langle u'^2 \rangle$ [figure 24(b)] where a low-momentum region was identified in the streamwise velocity defect near $z \approx 0.3\delta$. In contrast, the ensemble-averaged wall-normal Reynolds normal stress, $\langle v'^2 \rangle^+$ (figure 25), and the spanwise Reynolds normal stress, $\langle w'^2 \rangle^+$ (figure 26), show much less large-scale coherence, indicating that their behavior is more locally governed by smaller spatial scales of the flow. Of interest, the $M = 5$ model appears to yield

Table 4: Ensemble- and area-averaged values of single-point statistics at $y = 0.047\delta$.

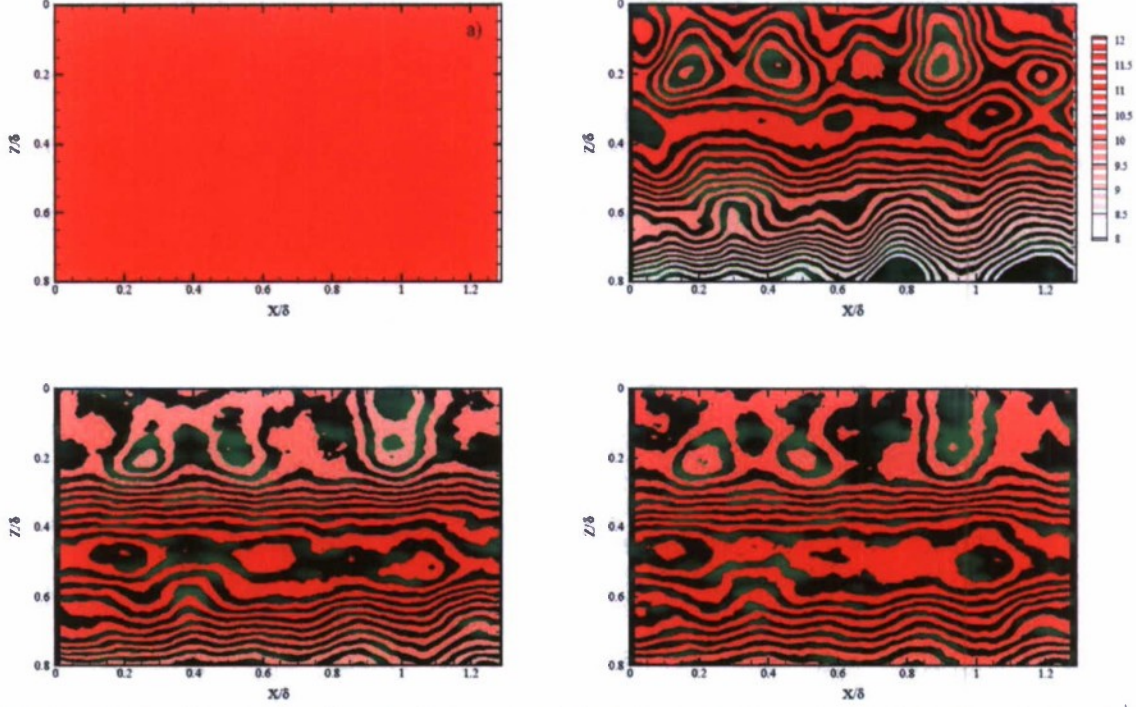| Surface	$\langle U_e - u \rangle^+$	$\langle u'^2 \rangle^+$	$\langle v'^2 \rangle^+$	$\langle u'v' \rangle^+$
Full	10.7	4.6	1.4	-0.96
$M = 16$	10.3	4.8	1.4	-1.00
$M = 5$	10.0	4.9	1.3	-0.98
Smooth	11.8	4.7	1.7	-0.88

Figure 22: Contour maps of ensemble-averaged streamwise velocity in defect scaling, $\langle U_e - u \rangle^+$, at $y = 0.047\delta$. (a) Smooth; (b) $M = 5$ model; (c) $M = 16$ model; (d) Full surface. Green background contours highlight local roughness topography beneath the wall-parallel measurement plane.

slightly larger magnitudes of both $\langle v'^2 \rangle^+$ and $\langle w'^2 \rangle^+$ compared to the $M = 16$ model and the full-surface results. In contrast, $\langle v'^2 \rangle^+$ and $\langle w'^2 \rangle^+$ for the $M = 16$ model and the full surface match one-another well both in magnitude as well as in spatial pattern.

A large-scale spatial pattern similar to that observed in the $\langle u'^2 \rangle^+$ is also noted in the ensemble-averaged Reynolds shear stress, $\langle u'v' \rangle^+$ (figure 27), where streamwise-elongated regions of intense $\langle u'v' \rangle^+$ sit near $z \approx 0.35\delta$ and $z \approx 0.65\delta$ in the $M = 16$ and full-surface results while a region of weaker $\langle u'v' \rangle^+$ is observed in-between. This region of weaker $\langle u'v' \rangle^+$ occurs spatially coincident to the low-momentum region noted in $\langle U_e - u \rangle^+$ while the two intense regions of $\langle u'v' \rangle^+$ lie along the boundaries of this low-momentum region. This imprint is also apparent in the ensemble-averaged Reynolds shear stress component $\langle u'w' \rangle^+$ as presented in figure 28. While the smooth-wall baseline [figure 28(a)] is nearly zero, as one would expect, $\langle u'w' \rangle^+$ is found to be intense in all three rough-wall cases with streamwise-elongated regions of positive and negative $\langle u'w' \rangle^+$ occurring along the boundaries of the low-momentum regions identified in $\langle U_e - u \rangle^+$. For example, the $M = 16$ and full-surface $\langle u'w' \rangle^+$ are positive in a streamwise-elongated region near $z \approx 0.35\delta$ and negative near $z \approx 0.65\delta$. These streamwise-elongated regions occur spatially coincident to similar elongated regions noted in $\langle u'^2 \rangle^+$ and
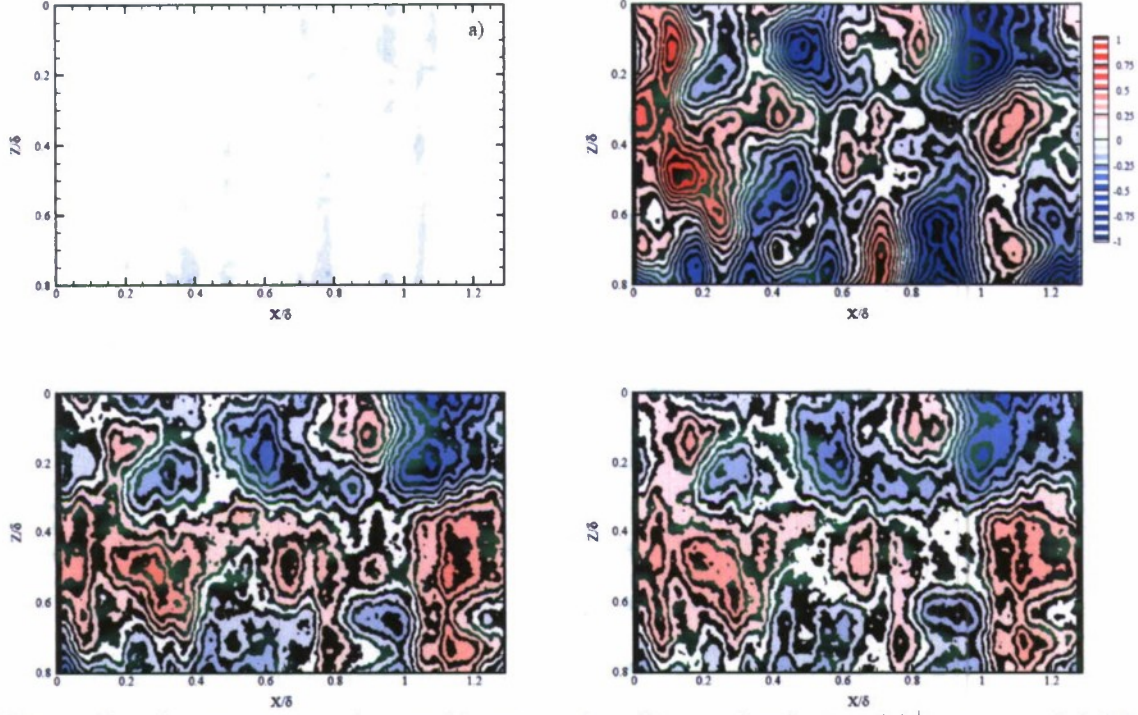
29

Figure 23: Contour maps of ensemble-averaged wall-normal velocity, $\langle v \rangle^+$, at $y = 0.047\delta$. (a) Smooth; (b) $M = 5$ model; (c) $M = 16$ model; (d) Full surface. Green background contours highlight local roughness topography beneath the wall-parallel measurement plane.

$\langle u'v' \rangle^+$.

5.3 Quadrant analysis

As discussed in section 3 and as applied to the PIV data in the streamwise–wall-normal plane (figures 11, 12, 16 and 17), quadrant analysis can be utilized to uncover the dominant Reynolds-shear-stress-producing patterns for flow over the two low-order models and the full surface from the streamwise–spanwise plane data deep within the roughness sublayer. For brevity, only the results for a threshold of $H = 4$ are shown in figure 29 for the $M = 5$ and $M = 16$ models as well as the full surface for ejection (Q_2) and sweep (Q_4) events. Unlike the mean RSS in figure 27 wherein streamwise-elongated regions of $\langle u'v' \rangle$ are readily apparent along the boundaries of the low-momentum regions identified in the mean velocity defect plots of figure 22, no such large-scale features are evident in either the ejection or sweep contributions to the mean Reynolds shear stress for intense events corresponding to a threshold of $H = 4$. Thus, these intense Reynolds-shear-stress-producing events are likely due to smaller-scale events that are intimately tied to the local roughness topography.

5.4 Vortical activity

Given the streamwise-elongated imprints noted in the mean velocity defect ($\langle U_e - u \rangle^+$; figure 22) as well as the streamwise Reynolds normal stress ($\langle u'^2 \rangle^+$; figure 24) and the Reynolds shear stress ($\langle u'v' \rangle^+$; figure 27), it is of interest to assess whether enhanced vortical activity might be responsible for these increased turbulence levels in the rough-wall flows. To make such an assessment, a vortex identifier termed swirling strength, λ_{ci}, is utilized to identify local rotational motions in the instantaneous velocity fields for each surface condition in the streamwise–spanwise measurement plane. Swirling strength is the imaginary portion of the complex eigenvalue of the local velocity gradient tensor and is an unambiguous marker of rotation [45, 46]. Unfortunately,
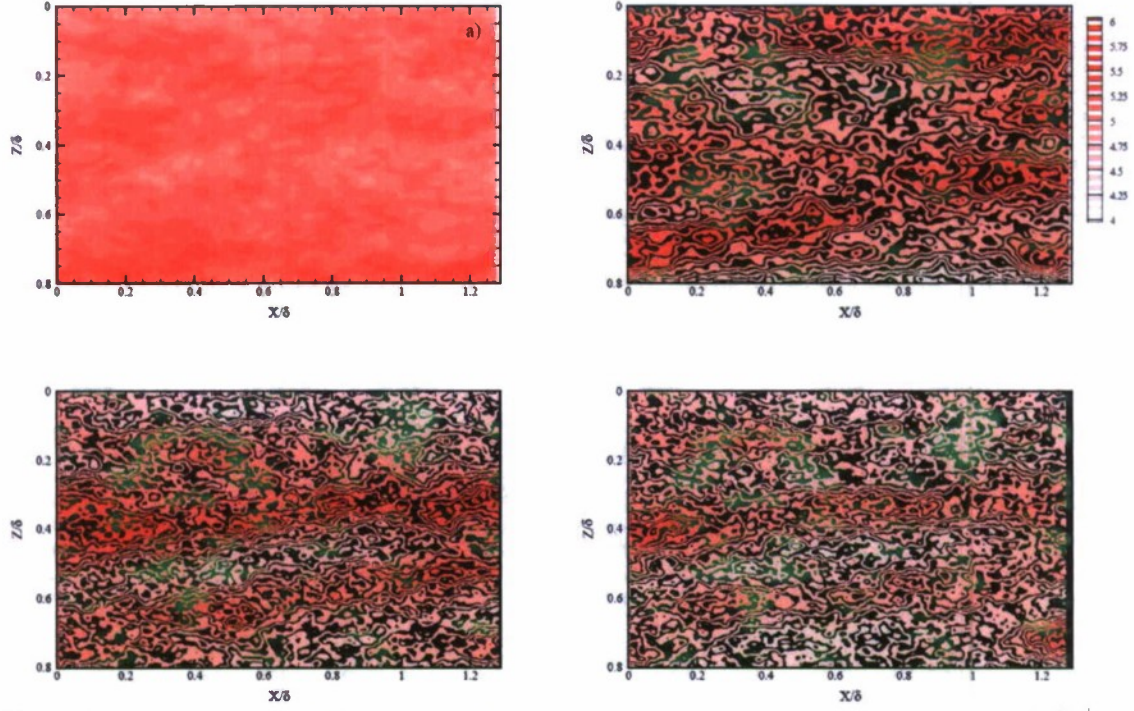
Figure 24: Contour maps of ensemble-averaged streamwise Reynolds normal stress, $\langle u'^2 \rangle^+$, at $y = 0.047\delta$. (a) Smooth; (b) $M = 5$ model; (c) $M = 16$ model; (d) Full surface. Green background contours highlight local roughness topography beneath the wall-parallel measurement plane.

λ_{ci} does not embody the sense of the rotation as the complex eigenvalues occur in complex-conjugate pairs, so λ_{ci} is assigned the sign of the local wall-normal vorticity as $\lambda_{ci}\omega_y/|\omega_y|$ so that clockwise-rotating vortices ($\omega_y < 0$) in the streamwise–spanwise measurement plane can be distinguished from counter-clockwise-rotating vortices ($\omega_y > 0$).

Figure 30 presents contour maps of ensemble-averaged $\lambda_{ci}\omega_y/|\omega_y|$ for the $M = 5$ and $M = 16$ models as well as the full surface. While the ensemble-averaged $\lambda_{ci}\omega_y/|\omega_y|$ for smooth-wall flow is essentially zero (not shown for brevity), indicative of no preferential locations for clockwise- and counter-clockwise-rotating wall-normal vortices, it displays clear preferential locations for such structures in all three rough-wall cases. Focusing on the $M = 16$ model and the full surface, recall that a clear low-momentum region existed near $z \approx 0.5\delta$. The ensemble-averaged $\lambda_{ci}\omega_y/|\omega_y|$ for these two cases display elongated regions of $\lambda_{ci}\omega_y/|\omega_y| < 0$ above and $\lambda_{ci}\omega_y/|\omega_y| > 0$ below this location with a region of $\lambda_{ci}\omega_y/|\omega_y| \approx 0$ between. This pattern in both the $M = 16$ model and full surface is consistent with a preferential alignment of clockwise-rotating wall-normal vortices along the upper boundary of the low-momentum region as well a preferential alignment of counter-clockwise-rotating wall-normal vortices below this low-momentum region. The combined induction of such vortical alignments will generate flow against the mean-flow direction and thus is consistent with the existence of a low-momentum region between these vortex paths. Recalling that the spatial signature of hairpin vortex packets in streamwise–spanwise measurement planes yields a qualitatively similar effect, particularly the existence of spanwise-separated counter-rotating wall-normal vortices between which a region of streamwise momentum deficit exists, these patterns in ensemble-averaged $\lambda_{ci}\omega_y/|\omega_y|$ may be indicative of a preferential alignment of such structures due to the roughness below the measurement plane or the generation of such structures directly by the roughness. Regardless of the origin, this evidence supports that vortical structures are likely responsible for the streamwise-elongated character of the mean velocity defect as well as certain components of the Reynolds stresses deep within the roughness sublayer.
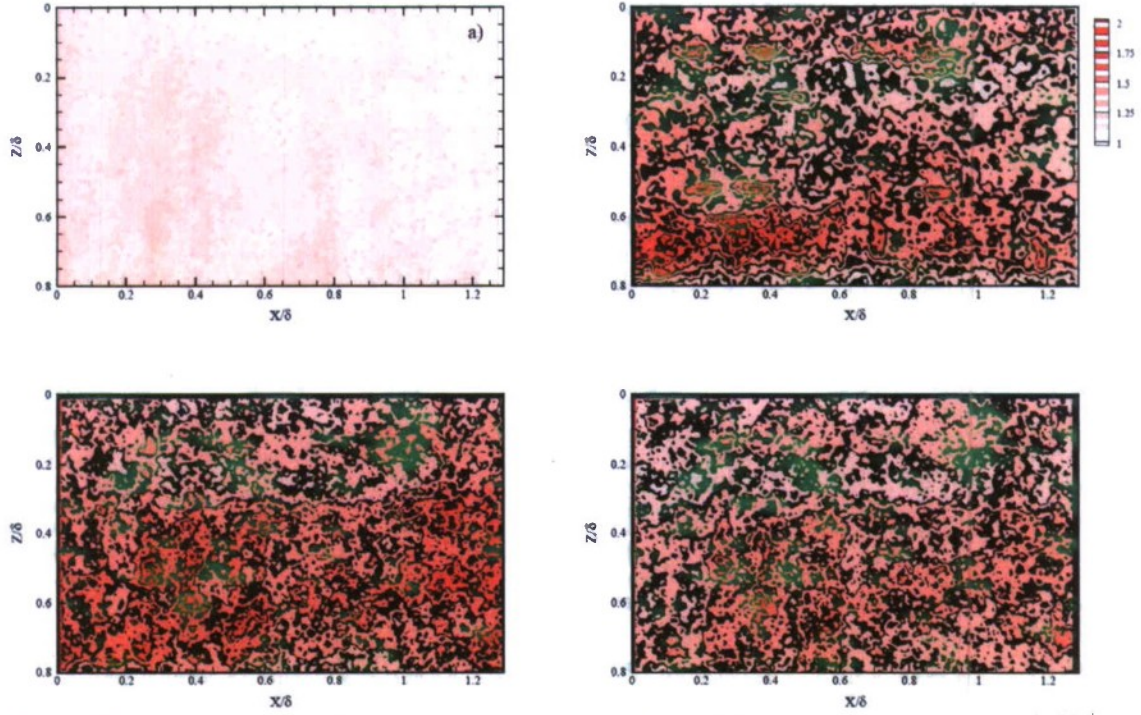
Figure 25: Contour maps of ensemble-averaged wall-normal Reynolds normal stress, $\langle v'^2 \rangle^+$, at $y = 0.047\delta$. (a) Smooth; (b) $M = 5$ model; (c) $M = 16$ model; (d) Full surface. Green background contours highlight local roughness topography beneath the wall-parallel measurement plane.
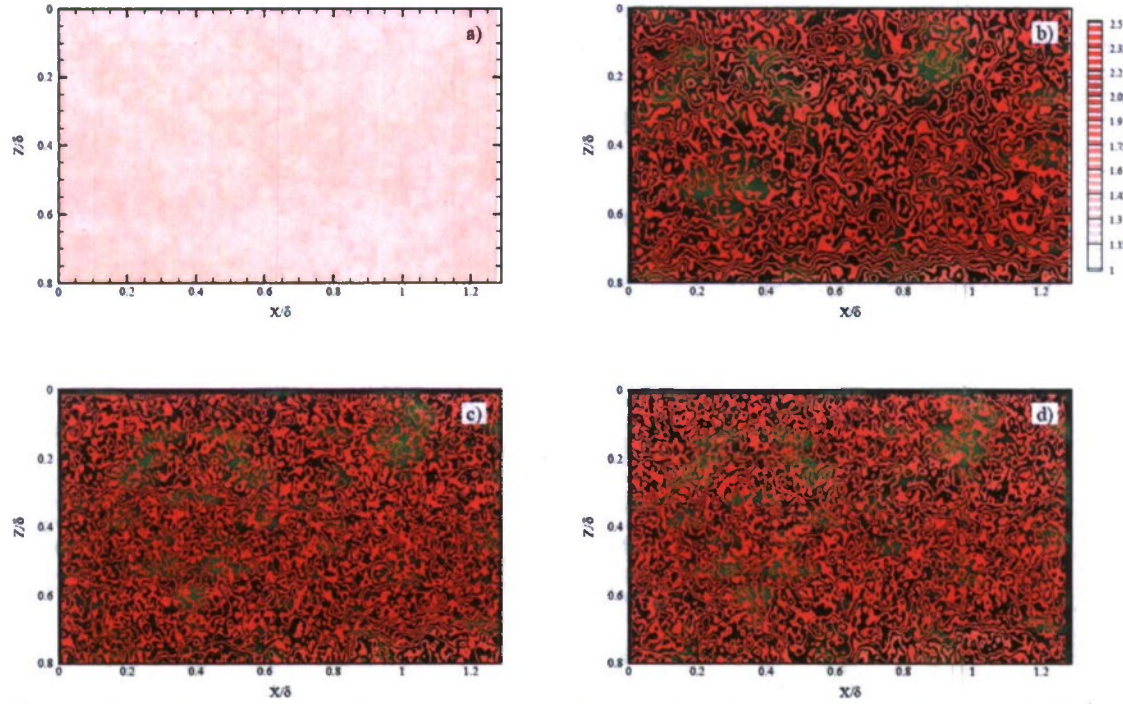

Figure 26: Contour maps of ensemble-averaged spanwise Reynolds normal stress, $\langle w'^2 \rangle^+$, at $y = 0.047\delta$. (a) Smooth; (b) $M = 5$ model; (c) $M = 16$ model; (d) Full surface. Green background contours highlight local roughness topography beneath the wall-parallel measurement plane.
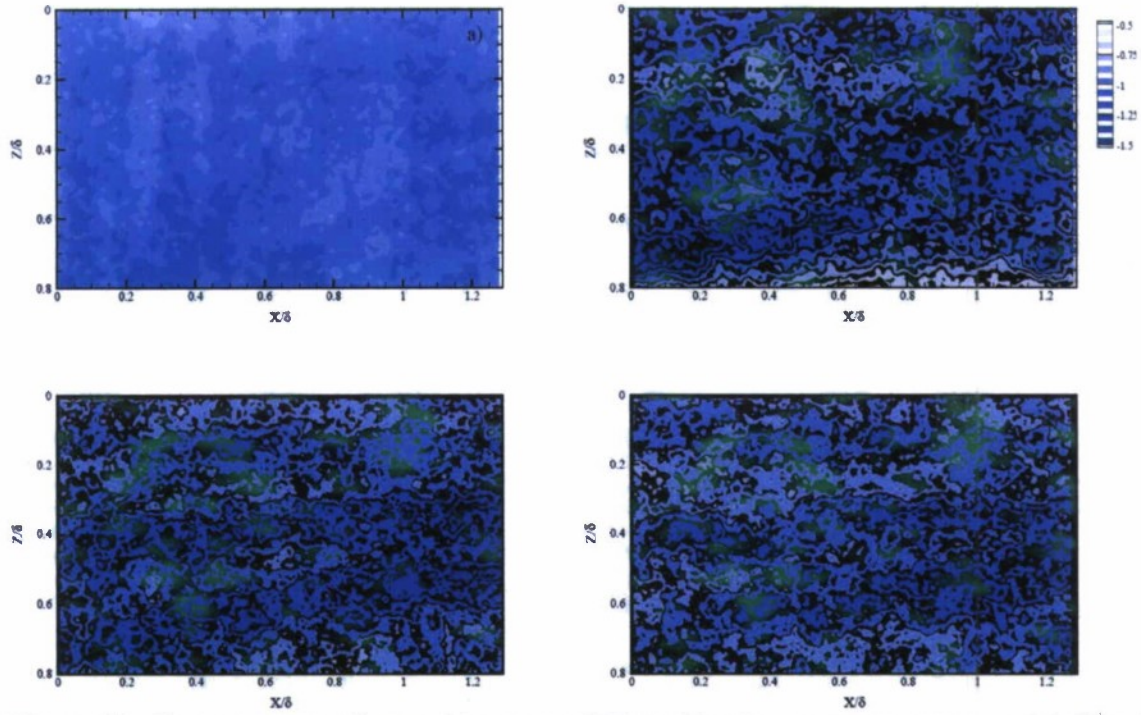
Figure 27: Contour maps of ensemble-averaged Reynolds shear stress component $\langle u'v'\rangle^+$ at $y = 0.047\delta$. (a) Smooth; (b) $M = 5$ model; (c) $M = 16$ model; (d) Full surface. Green background contours highlight local roughness topography beneath the wall-parallel measurement plane.
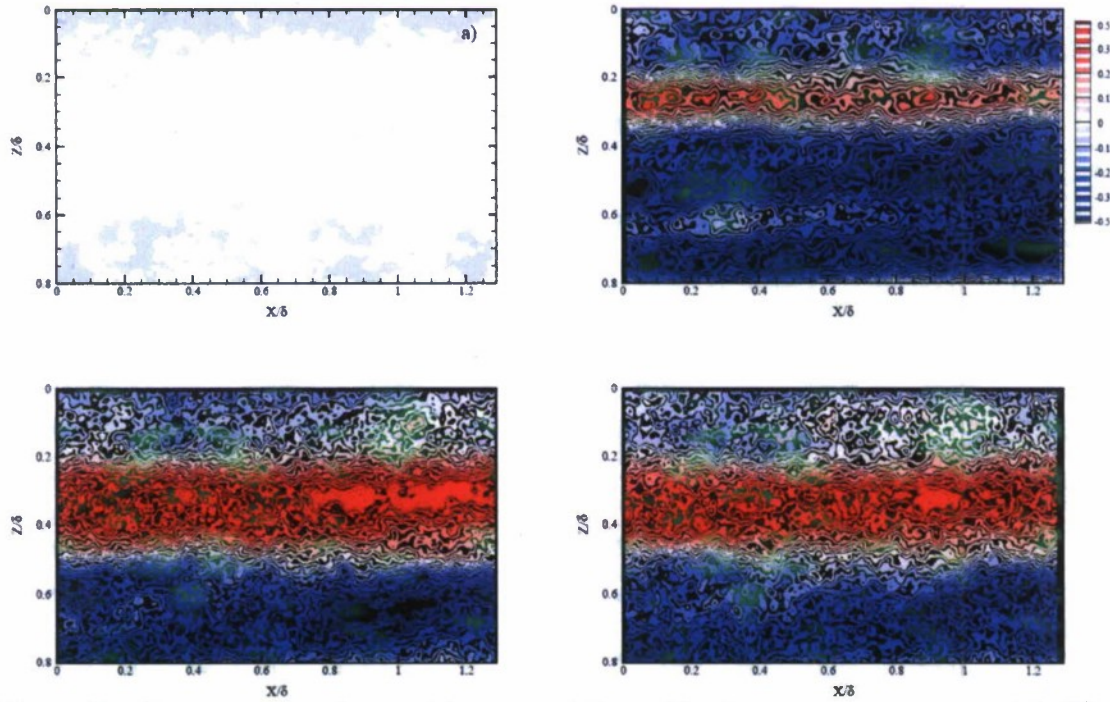

Figure 28: Contour maps of ensemble-averaged Reynolds shear stress component $\langle u'w'\rangle^+$ at $y = 0.047\delta$. (a) Smooth; (b) $M = 5$ model; (c) $M = 16$ model; (d) Full surface. Green background contours highlight local roughness topography beneath the wall-parallel measurement plane.
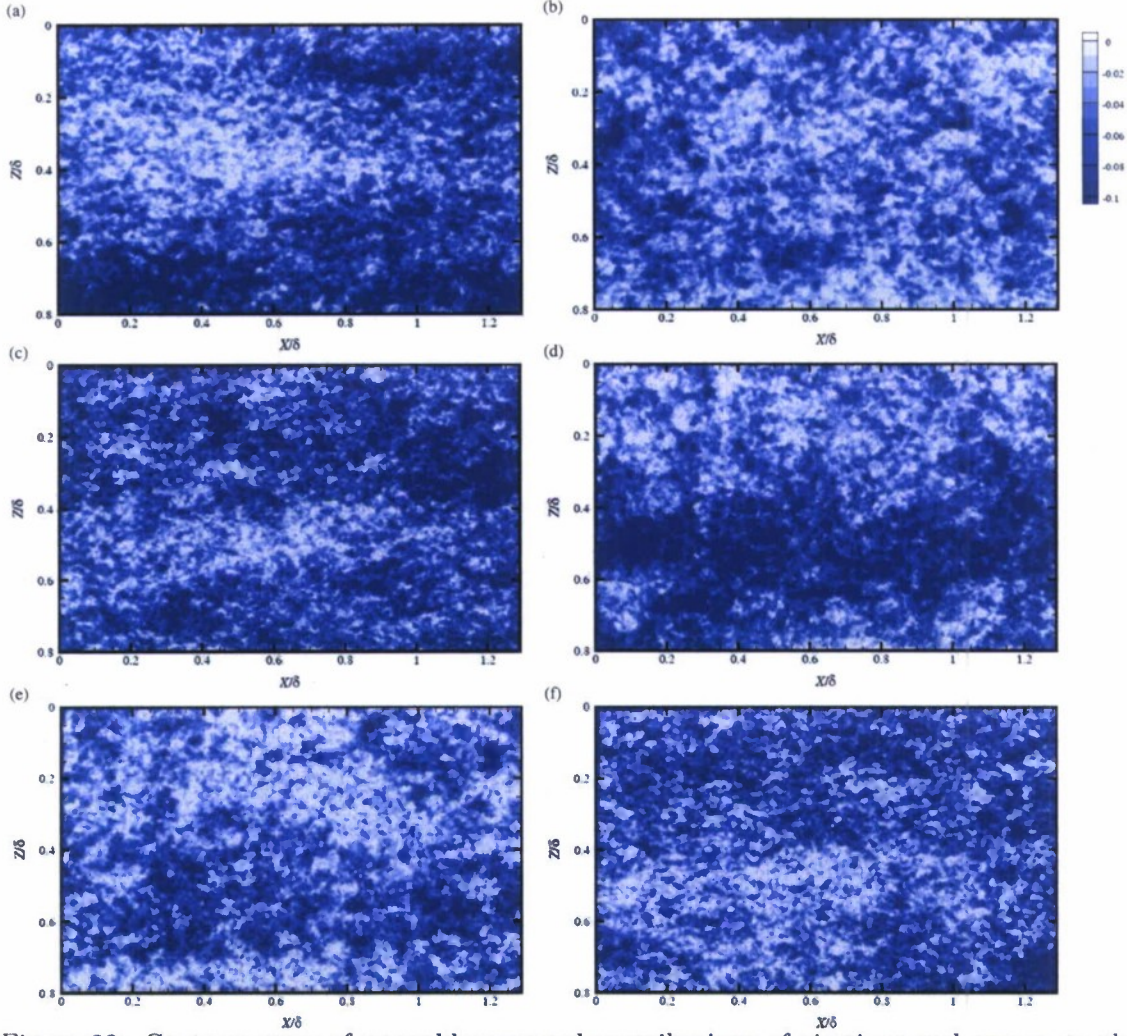
Figure 29: Contour maps of ensemble-averaged contributions of ejections and sweeps to the mean Reynolds shear stress with a threshold of $H = 4$ at $y = 0.047\delta$. (a,b) $M = 5$ model; (c,d) $M = 16$ model; (e,f) Full surface.

5.5 Two-point velocity correlation coefficients

Finally, two-point correlation coefficients of the three velocity components resolved in the streamwise–spanwise measurement plane are used to assess the average spatial structure of the flows in the $y = 0.047\delta$ measurement plane within the roughness sublayer. Note that these correlations are computed assuming homogeneity in the streamwise direction but inhomogeneity in the spanwise (z) direction to assess the variations of these correlations on spanwise position. Figures 31(a) and 31(b) presents ρ_{uu} for the $M = 16$ model and the full surface flows, respectively, for a spanwise position coincident with the low-momentum region identified in the mean velocity defect for these two cases. Both results are quite elongated in the streamwise direction (the $\rho_{uu} = 0.3$ contour extends approximately δ, for example) and a region of weaker, negative correlation is evident outboard of the positive correlation region in the spanwise direction. The streamwise-elongated nature of ρ_{uu} in smooth-wall turbulence has been previously linked to the low-momentum regions generated by hairpin vortex packets and the negative correlation outboard of the positive region in the spanwise direction represent the imprint of spanwise-alternating low- and high-momentum regions. [47, 48] In addition, Wu and Christensen [48] recently reported similar characteristics of ρ_{uu} for flow over irregular roughness near the outer
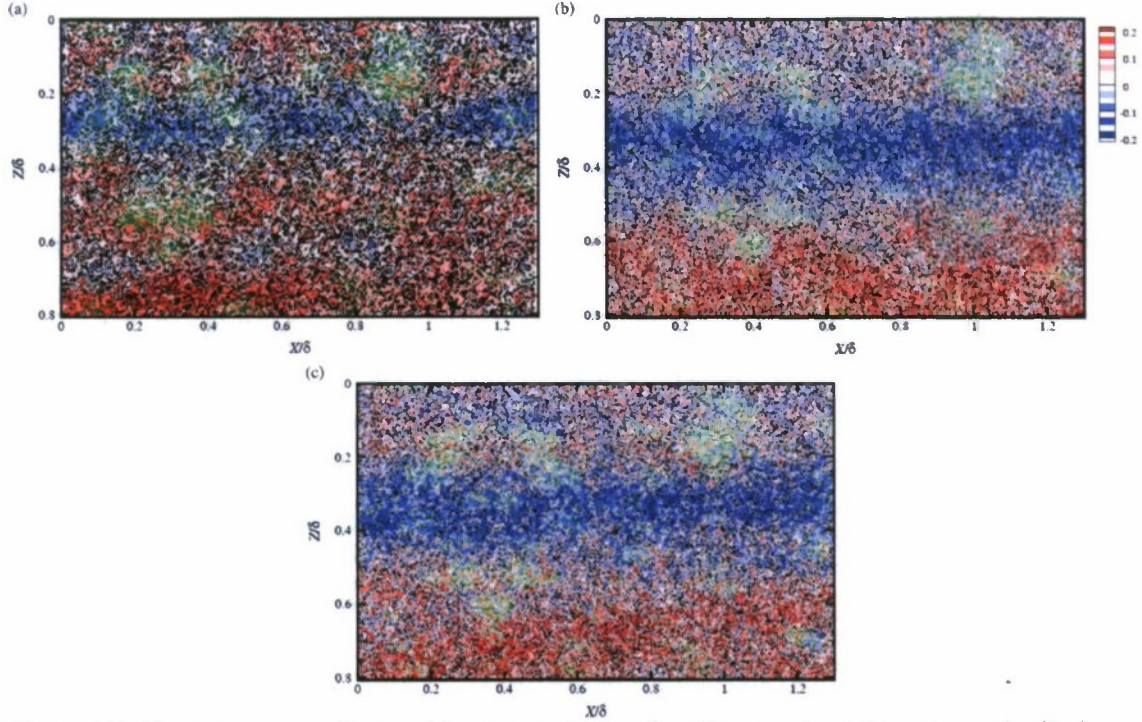
34

Figure 30: Contour maps of ensemble-averaged signed wall-normal swirling strength, $\langle \lambda_{ci} \rangle$ normalized by u_τ and δ at $y = 0.047\delta$. (a) $M = 5$ model; (b) $M = 16$ model; (c) Full surface. Green background contours highlight local roughness topography beneath the wall-parallel measurement plane.

edge of the roughness sublayer, supporting the relative immunity of these vortical structures as well as their coherent organization into larger-scale structural entities to roughness. The present results lend additional support to the contention that hairpin vortex packets exist in rough-wall turbulence as well, including at the wall-normal position of the present measurements ($y = 0.047\delta$) which is deep within the roughness sublayer where roughness effects are most dramatic.

Interestingly, the characteristic streamwise and spanwise spatial scales of the $M = 16$ ρ_{uu} match those of the full surface extremely well. The only notable difference lies in the regions of negative correlation which are more streamwise-elongated in the full-surface flow than in the $M = 16$ result. Nevertheless, the consistency between the $M = 16$ and full-surface results highlight the ability of the $M = 16$ model to reproduce the average structural characteristics of the full-surface flow despite not containing the smaller-scale topographical details of the full surface. For reference, the $M = 5$ ρ_{uu} computed on the low-momentum region identified in its mean velocity defect at $z \approx 0.3\delta$ shows similar streamwise elongation as well as spanwise-offset regions of negative correlation, but it is not included here since this spanwise position does not coincide with that of the $M = 16$ and full surface low-momentum regions.

Figures 32(a) and 32(b) present two-point correlation coefficients of wall-normal velocity, ρ_{vv}, for the $M = 16$ model and the full surface, respectively, at the same spanwise location as ρ_{uu} (i.e., coincident with the spanwise position of the low-momentum regions identified in their respective mean velocity defects). Previous studies have shown that ρ_{vv} is much smaller in spatial scale than ρ_{uu} and is thus more consistent with the imprint of the individual vortices present in the flow than with the streamwise alignment of such structures into larger-scale packets. [47, 48] In addition, Wu and Christensen [48] recently reported the smaller spatial scales of the flow to be quite insensitive to roughness effects as reflected in consistency between smooth- and rough-wall ρ_{vv} near the outer edge of the roughness sublayer. A similar consistency
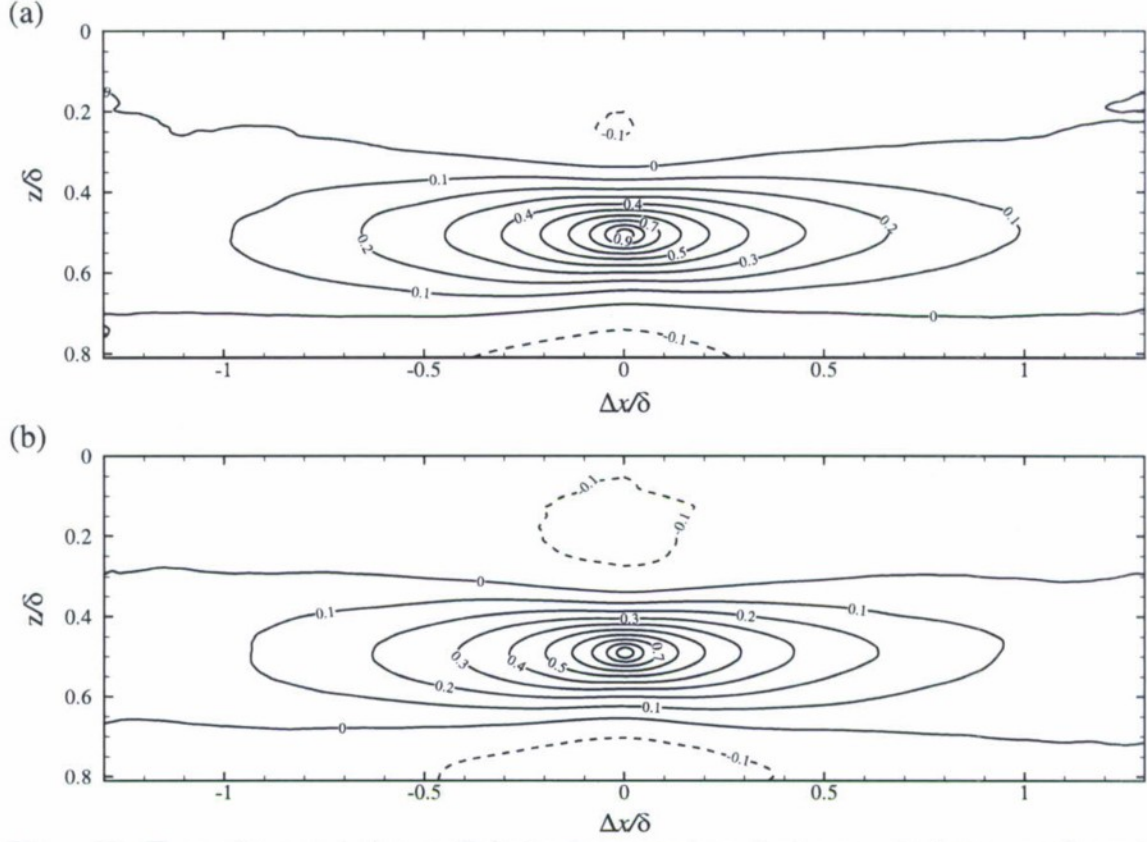
Figure 31: Two-point correlation coefficients of streamwise velocity, ρ_{uu}, in the $x-z$ plane at $y = 0.047\delta$ at the spanwise position of the low-momentum region noted in the mean velocity defect (figure 22). (a) $M = 16$ model; (b) Full surface.

is noted herein between the $M = 16$ and full surface ρ_{vv} at $y = 0.047\delta$ as both are quite compact in the spanwise direction and show only a slight elongation in the streamwise direction, though nearly an order of magnitude smaller than ρ_{uu}. Thus, the $M = 16$ model is able to reproduce the average spatial characteristics of the vortical structures that populate the full-surface flow within the roughness sublayer quite well.

Figures 33(a) and 33(b) present two-point correlation coefficients of spanwise velocity, ρ_{ww}, for the $M = 16$ model and the full surface, respectively, again at the same spanwise location as ρ_{uu} and ρ_{vv}. A slight enhancement in the streamwise coherence of ρ_{ww} is noted in the $M = 16$ result compared to that of the full surface. Nevertheless, the general spatial characteristics of the full-surface ρ_{ww} are clearly reproduced by the $M = 16$ surface.

Figures 34(a) and 34(b) present the negative of two-point cross-correlation coefficients of streamwise and wall-normal velocity, $-\rho_{uv}$, for the $M = 16$ model and the full surface, respectively. Previous studies have found ρ_{uv} to reflect both the smaller-scale nature of ρ_{vv}, likely the imprint of individual Reynolds-shear-stress-producing events, as well as the larger-scale streamwise coherence of ρ_{uu} indicative of the collective induction of such events by the multiple vortices within hairpin vortex packets. [48] The present results are consistent with this behavior as $-\rho_{uv}$ is streamwise-elongated and contains spanwise-offset regions of negative correlation. The alternating sign of this correlation in the spanwise direction is regarded as the imprint of spanwise-alternating low- and high-momentum regions, the former of which have been previously found to embody strong ejection events while the latter embody strong sweep events. When comparing the $M = 16$ and full surface results, strong agreement is noted both in stream-wise and spanwise extent as well as in the magnitude of the correlation both in the positive and
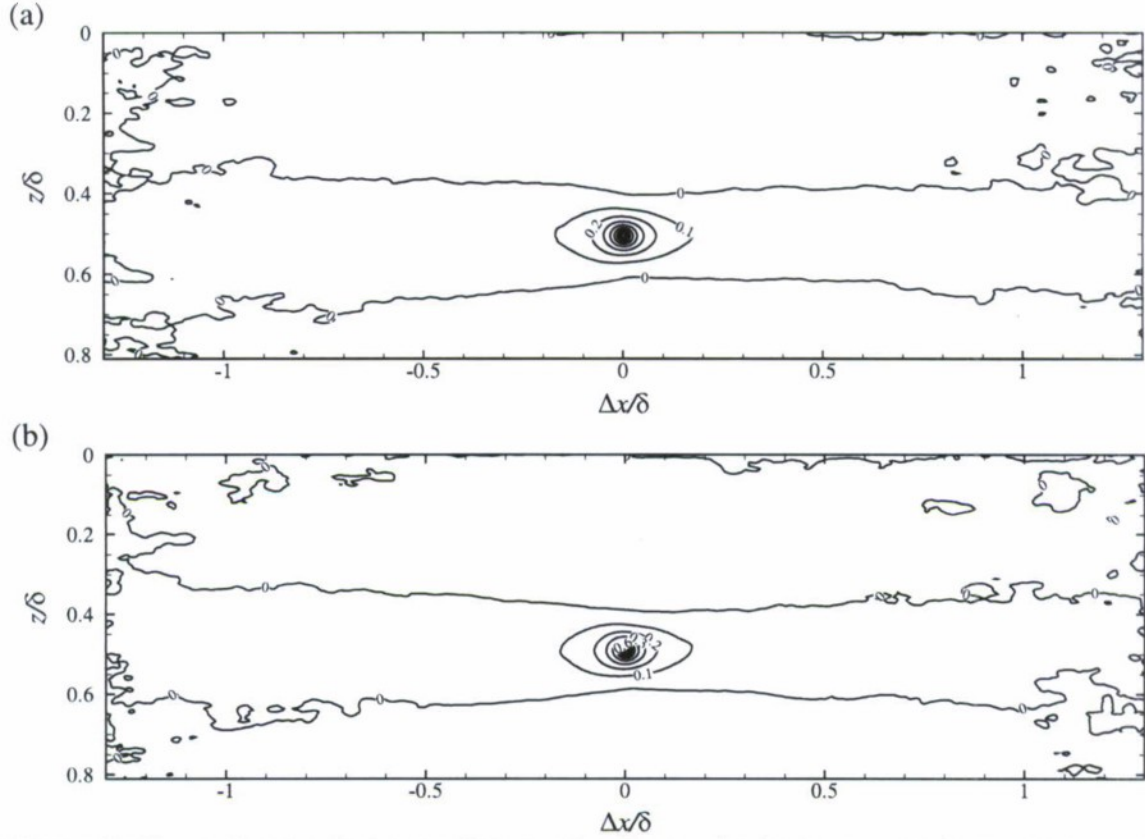
Figure 32: Two-point correlation coefficients of wall-normal velocity, ρ_{vv}, in the $x - z$ plane at $y = 0.047\delta$ at the spanwise position of the low-momentum region noted in the mean velocity defect (figure 22). (a) $M = 16$ model; (b) Full surface.

negative correlation regions. Thus, the $M = 16$ model reproduces the average spatial character of the dominant Reynolds-shear-stress-producing events of the full-surface flow quite well.

Finally, it should be noted that these correlation coefficients computed at other spanwise locations, including at the edges of the low-momentum regions identified in the mean velocity defect results as well as in identified regions of high momentum, display similar consistency between the $M = 16$ model and the full surface. As such, these results highlight the efficacy of the $M = 16$ model, containing the larger- and intermediate-scales of the full-surface topography, in reproducing the spatial structure of the full-surface flow deep within the roughness sublayer where the impact of roughness is the most obvious. While not shown, the $M = 5$ correlations show good qualitative consistency with the $M = 16$ and full-surface results; however, some, albeit somewhat weak, quantitative differences are notable, indicating that the intermediate topographical scales not captured by the $M = 5$ model have a measurable impact on the flow within the roughness sublayer.

6   Summary

Low-order representations of highly-irregular surface roughness replicated from a damaged turbine blade were tested in a zero-pressure-gradient turbulent boundary layer under both developing- and developed flow scenarios. For the case of developing flow, a model embodying the first 16 of 383 modes (4.2% of the total modes) which captures 95% of the full surface content accurately reproduces the flow characteristics of flow over the full surface, including the mean velocity profile, Reynolds normal and shear stresses, pdfs of RSS-producing events and quad-
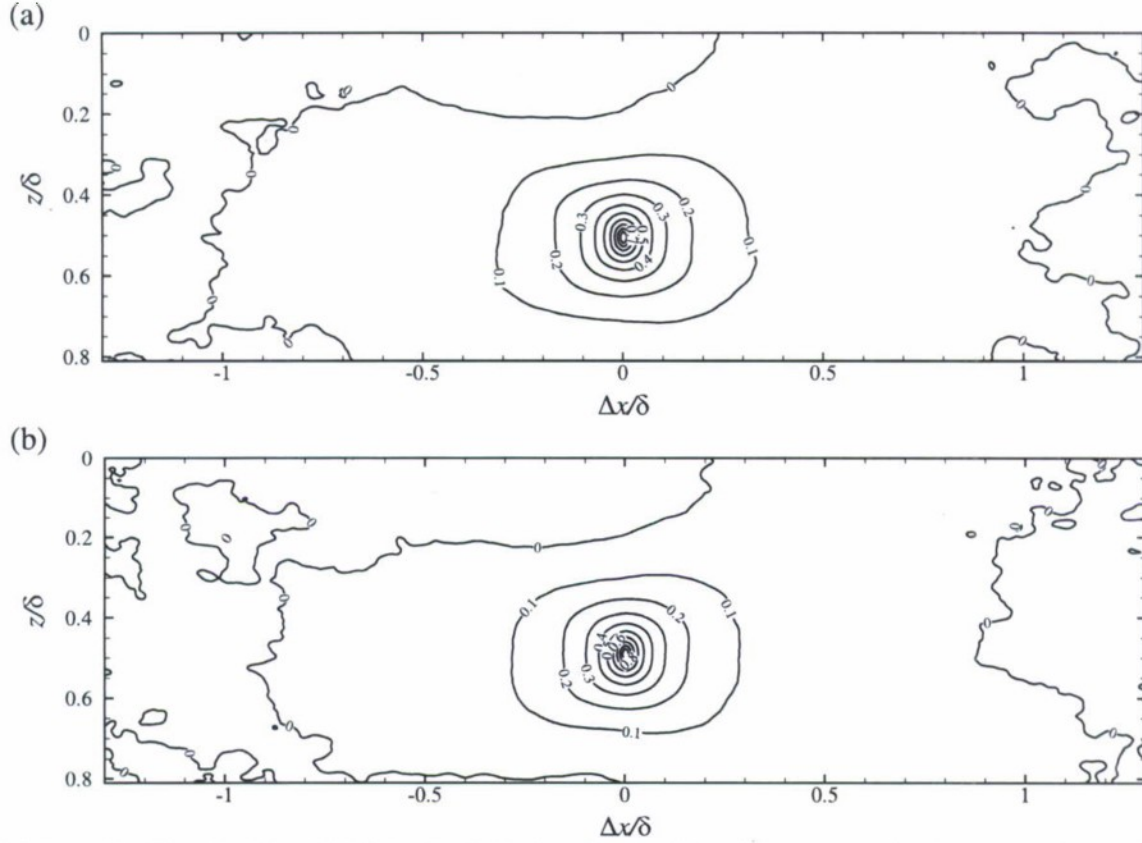
Figure 33: Two-point correlation coefficients of spanwise velocity, ρ_{ww}, in the $x - z$ plane at $y = 0.047\delta$ at the spanwise position of the low-momentum region noted in the mean velocity defect (figure 22). (a) $M = 16$ model; (b) Full surface.

rant contributions to the mean RSS. In contrast, a 5-mode surface model fails to reproduce the flow characteristics of the full surface despite containing 71% of the full-surface topographical content and having an RMS roughness height that is 84% that of the full surface.

For the case of developed flow, wherein the internal roughness layer has grown to engulf the entire boundary-layer thickness and a self-similar state is attained in all surface cases, both the 5- and 16-mode surface models faithfully reproduce the character of the full-surface flow outside the roughness sublayer, including both single- and multi-point statistics as well as important details of the instantaneous RSS-producing events as discerned from quadrant analysis. However, this consistency is a bit misleading due to the manner in which the flow statistics are scaled and compared (by u_τ and δ). In fact, since these flows have attained a self-similar state, this collapse is simply attributable to the existence of outer-layer similarity for the present surfaces in accordance with Townsend's wall similarity hypothesis. In fairness, neither the 5- nor 16-mode model fully-reproduces the bulk flow characteristics of the full-surface flow as represented by the downward shift in the mean velocity profile via the roughness function, ΔU^+, though the 16-mode model is quite close ($\Delta U^+ = 7.9$ compared to 8.2 for the full-surface flow). Nevertheless, this observation of outer-layer similarity for the two low-order representations, the full surface and the smooth wall is actually quite important because it highlights the relatively weak impact that the intermediate- and finer-scale topographical details of the roughness have on the outer-layer flow. As such, for the topography under study herein, knowledge of simply u_τ and δ would provide accurate prediction of the outer-layer behavior of the full-surface and low-order-model flows from smooth-wall statistics.

In contrast, important differences are noted between flow over the 5- and 16-mode models
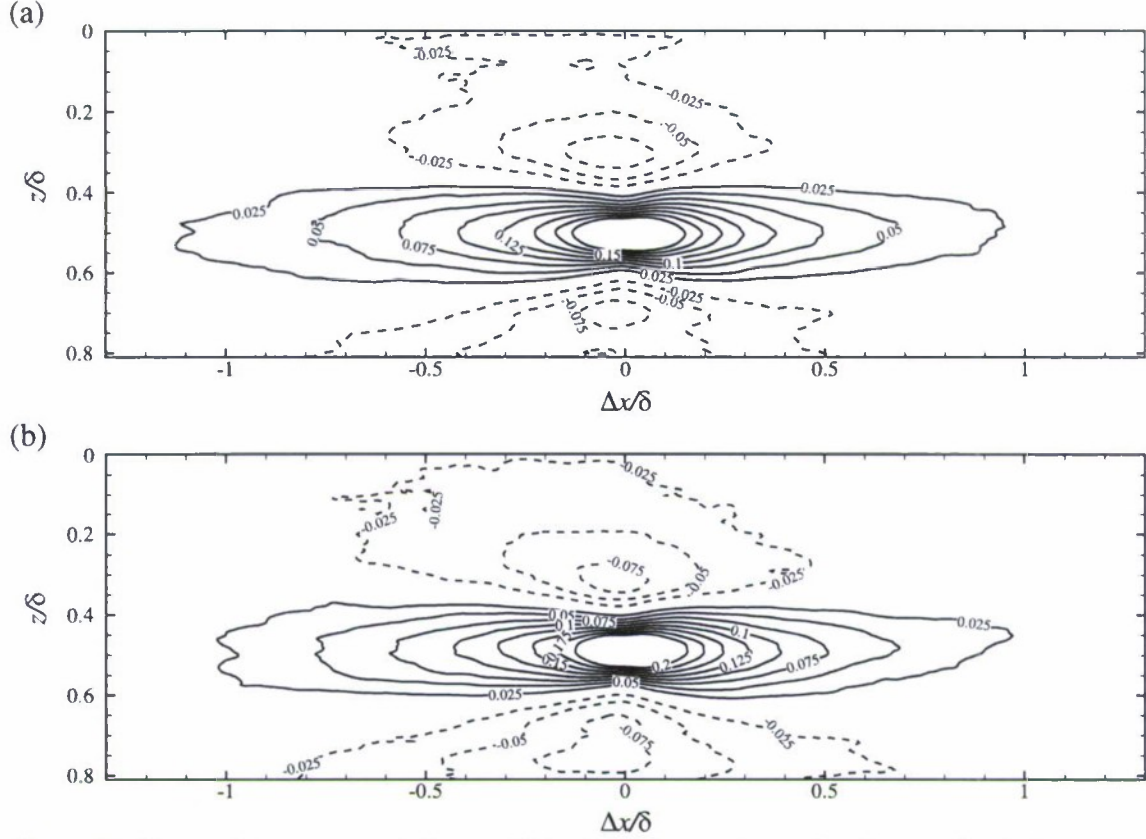
38

Figure 34: Two-point cross-correlation coefficients of streamwise and wall-normal velocity, $-\rho_{uv}$, in the $x - z$ plane at $y = 0.047\delta$ at the spanwise position of the low-momentum region noted in the mean velocity defect (figure 22). (a) $M = 16$ model; (b) Full surface.

and the full surface within the roughness sublayer where the details of the roughness are expected to play a pivotal role in the flow development. In particular, both the 5- and 16-mode models yield lower values of $\langle u'^2 \rangle$ in the roughness sublayer compared to the full-surface case. Similarly, these models fail to reproduce the contributions of intense ejection and sweep events noted in the roughness sublayer of the full-surface flow. Further, both low-order surface representations produce an enhanced shortening in the streamwise extent of the two-point correlation of streamwise velocity compared to the full-surface flow. Taken together, these observations from the streamwise–wall-normal plane PIV measurements indicate that finer-scale topographical scales of the roughness play subtle, but measurable, roles in the overall flow development within the roughness sublayer for the topography considered. In this regard, it was noted that these finer-scale topographical details captured in the truncated higher-order SVD modes embody important details regarding the jagged edges of the large-scale protrusions. Thus, the observed differences within the roughness sublayer for the two surface models compared to that of the full-surface flow reflect the importance of these topographical details in the near-surface flow, possibly through modifications of the separation behavior downstream of large-scale protrusions and/or vortex shedding from these features.

The measurements in a streamwise–spanwise plane deep within the roughness sublayer at $y = 0.047\delta$ highlight how flow within the roughness sublayer for all three rough-wall cases clearly depends upon the local roughness topography. In particular, the full surface and the $M = 16$ model, which closely resembles the full-surface topography, both produce similar regions of streamwise momentum deficit that are bounded by intense regions of $\langle u'^2 \rangle$, $\langle u'v' \rangle$ and $\langle u'w' \rangle$. These patterns indicate that the local roughness features can generate significant heterogeneities

39

in the turbulence statistics that might reflect preferential regions of enhanced turbulence production and possibly dissipation. Understanding such processes is crucial for the development of turbulence models that can properly capture the local impact of surface roughness on energy generation, redistribution and dissipation.

Finally, the efficacy of the $M = 16$ surface model in reproducing many of the characteristics of flow over the full surface considered herein is quite interesting and provides some insight into the roughness characteristics that have the greatest impact on the flow. However, this particular level of modal content cannot be viewed as a universal requirement for constructing models of other irregular rough surfaces. Of interest, though, is the fact that the fractional surface content of 95% for the $M = 16$ surface model in this effort is consistent with that noted in the recent study of Johnson and Christensen [33] wherein a very different realistic rough surface was reconstructed with 95% of the fractional surface content using the first 20 SVD modes of the topographical decomposition. Consistency was noted with flow over the full surface under developing-flow conditions except in the very near-wall region. Thus, while the number of SVD basis functions included in a topographical model will most certainly vary from surface to surface, these two efforts highlight the possibility that fractional surface content might provide at least partial guidance in determining the appropriate modal content for low-order models of irregular roughness. Further study of a range of realistic rough surfaces is needed to critically assess this possibility.

7 Resulting Publications

7.1 Archival papers and conference proceedings

Mejia-Alvarez, R. & Christensen, K. T. 2010. Low-Order Representations of Irregular Surface Roughness and Their Impact on a Turbulent Boundary Layer. *Phys. Fluids*, **22** (1), 015106 (20 pp).

Johnson, B. & Christensen, K. T. 2009. Turbulent Flow Over Low-Order Models of Highly-Irregular Surface Roughness. *AIAA J.*, **47** (5), 1288-1299.

Mejia-Alvarez, R. & Christensen, K. T. 2010. Low-Order Representations of Irregular Surface Roughness and Their Impact on a Turbulent Boundary Layer. *16th U.S. National Congress of Theoretical and Applied Mechanics Conference*, USNCTAM2010-568.

Mejia-Alvarez, R. & Christensen, K. T. 2010. Impact of Low-Order Representations of Irregular Surface Roughness on Flow in the Roughness Sublayer. *40th AIAA Fluid Dynamics Conference*, AIAA Paper 2010-5018.

Mejia-Alvarez, R. & Christensen, K. T. 2009. Flow of Turbulent Boundary Layers Over Low-Order Representations of Irregular Surface Roughness. *39th AIAA Fluid Dynamics Conference*, AIAA Paper 2009-3681.

Mejia-Alvarez, R., Wu, Y. & Christensen, K. T. 2009. Modifications of the Structure of Turbulent Flow by a Rough Surface. *47th AIAA Aerospace Sciences Meeting*, AIAA Paper 2009-0399.

Johnson, B. & Christensen, K. T. 2008. Low-Order Models of Highly-Irregular Surface Roughness. *38th AIAA Fluid Dynamics Conference*, AIAA Paper 2008-3961.

7.2 Theses

Mejia-Alvarez, R. 2010. Low-Order Models of Irregular Surface Roughness and Their Impact on a Turbulent Boundary Layer. Ph.D. Thesis, Mechanical Science and Engineering Department, University of Illinois, Urbana, IL, to be defended August 2010.

7.3 Unpublished conference presentations

Mejia-Alvarez, R. & Christensen, K. T. 2009. Flow of Turbulent Boundary Layers Over Low-Order Representations of Irregular Surface Roughness, *62nd APS-DFD Meeting*.

Mejia-Alvarez, R., Wu, Y. & Christensen, K. T. 2008. Observations of Large-Scale Meandering Motions in Rough-Wall Turbulence, *61st APS-DFD Meeting*.

8 Acknowledgements

References

[1] J.P. Bons, R.P. Taylor, S.T. McClain, and R.B. Rivir. The many faces of turbine surface roughness. *Journal of Turbomachinery*, 123:739–748, 2001.

[2] J.P. Bons. St and C_f augmentation for real turbine roughness with elevated freestream turbulence. *Journal of Turbomachinery*, 124:632–644, 2002.

[3] R.I. Karlsson. *Studies of Skin Fiction in Turbulent Boundary Layers on Smooth and Rough Walls*. PhD thesis, Chalmers Institue of Technology, Göteborg, Sweden, 1980.

[4] J. Nikuradse. Laws of flow in rough pipes. *NACA Technical Memorandum*, (1292), 1933.

[5] C. F. Colebrook and C. M. White. Experiments with fluid friction in roughened pipes. *Proc. R. Soc. London, Ser. A*, 161:367, 1937.

[6] C. F. Colebrook. Turbulent flow in pipes with particular reference to the transition region between the smooth- and rough-wall laws. *J. Inst. Civil Eng.*, 11:133–56, 1939.

[7] A. J. Smits and D. H. Wood. The response of turbulent boundary layers to sudden perturbations. *Ann. Rev. Fluid Mech.*, 17:321–58, 1985.

[8] R. A. Antonia and R. E Luxton. The response of a turbulent boundary layer to a step change in surface roughness. Part 1. Smooth to rough. *J. Fluid Mech.*, 48:721–761, 1971.

[9] J. Andreopoulos and D. H Wood. The response of a turbulent boundary layer to a short length of surface roughness. *J. Fluid Mech.*, 118:143–164, 1982.

[10] W. H. Schofield. Measurements in adverse-pressure-gradient turbulent boundary layers with a step change in surface roughness. *J. Fluid Mech.*, 112:573–593, 1990.

[11] Y. Wu and K.T. Christensen. Reynolds-stress enhancement associated with a short fetch of roughness in wall turbulence. *American Institute of Aeronautics and Astronautics Journal*, 44:3098–3106, 2006.

[12] A. J. Grass. Structural features of turbulent flow over smooth and rough boundaries. *J. Fluid Mech.*, 50:233–255, 1971.

[13] M. R. Raupach. Conditional statistics of Reynolds stress in rough-wall and smooth-wall turbulent boundary layers. *J. Fluid Mech.*, 108:363–382, 1981.

[14] P. M. Ligrani and R. J. Moffat. Structure of transitionally rough and fully rough turbulent boundary layers. *J. Fluid Mech.*, 162:69–98, 1986.

[15] P. R. Bandyopadhyay and R. D. Watson. Structure of rough-wall turbulent boundary layers. *Phys. Fluids*, 31:1877–1883, 1988.

[16] A. E. Perry and J. D. Li. Experimental support for the attached-eddy hypothesis in zero-pressure-gradient turbulent boundary layers. *J. Fluid Mech.*, 218:405–438, 1990.

[17] M. P. Schultz and K. A. Flack. Turbulent boundary layers over surfaces smoothed by sanding. *J. Fluids Eng.*, 125:863–870, 2003.

[18] M. P. Schultz and K. A. Flack. Outer layer similarity in fully rough turbulent boundary layers. *Exp. Fluids*, 38:328–340, 2005.

[19] K. A. Flack, M. P. Schultz, and T. A. Shapiro. Experimental support for Townsend's Reynolds number similarity hypothesis on rough walls. *Phys. Fluids*, 17:035102, 2005.

[20] M. P. Schultz and K. A. Flack. The rough-wall turbulent boundary layer from the hydraulically smooth to the fully rough regime. *J. Fluid Mech.*, 580:381–405, 2007.

[21] R. J. Volino, M. P. Schultz, and K. A. Flack. Turbulence structure in rough- and smooth-wall boundary layers. *J. Fluid Mech.*, 592:263–293, 2007.

[22] A. A. Townsend. *The Structure of Turbulent Shear Flow*. Cambridge University Press, 2nd edition, 1976.

[23] M. R. Raupach, R. A. Antonia, and S. Rajagopalan. Rough-wall turbulent boundary layers. *Appl. Mech. Rev.*, 44:1–25, 1991.

[24] J. Jimenez. Turbulent flow over rough walls. *Annu. Rev. Fluid Mech.*, 36:173, 2004.

[25] J. J. Allen, M. A. Shockling, G. J. Kunkel, and A. J. Smits. Turbulent flow in smooth and rough pipes. *Phil. Trans. R. Soc. A*, 365:699–714, 2007.

[26] Y. Wu and K.T. Christensen. Outer-layer similarity in the presence of a practical rough-wall topography. *Physics of Fluids*, 19:085108, 2007.

[27] P. A. Krogstad, R. A. Antonia, and L. W. B. Browne. Comparison between rough and smooth-wall turbulent boundary layers. *J. Fluid Mech.*, 245:599–617, 1992.

[28] P. A. Krogstad and R. A. Antonia. Structure of turbulent boundary layers on smooth and rough walls. *J. Fluid Mech.*, 277:1–21, 1994.

[29] L. Keirsbulck, L. Labraga, A. Mazouz, and C. Tournier. Surface roughness effects on turbulent boundary layer structures. *J. Fluids Eng.*, 124:127–135, 2002.

[30] K. Bhaganagar, J. Kim, and G. Coleman. Effect of roughness on wall-bounded turbulence. *Flow, Turbulence and Combustion*, 72:463–492, 2004.

[31] M.P. Schultz and K.A. Flack. Outer layer similarity in fully rough turbulent boundary layers. *Experiments in Fluids*, 38:328–340, 2005.

[32] M. Itoh, S. Tamano, R. Iguchi, K. Yokota, N. Akino, R. Hino, and S. Kubo. Turbulent drag reduction by the seal fur surface. *Phys. Fluids*, 18(065102):1–9, 2006.

[33] B.E. Johnson and K.T. Christensen. Turbulent flow over low-order models of highly-irregular surface roughness. *American Institute of Aeronautics and Astronautics Journal*, 47:1288–1299, 2009.

[34] C. D. Meinhart. *Investigation of Turbulent Boundary-Layer Structure using Particle-Image Velocimetry*. PhD thesis, Department of Theorretical and Applied Mechanics, University of Illinois at Urbana-Champaign, 1994.

[35] Y. Wu and K. T. Christensen. Outer-layer similarity in the presence of a practical rough-wall topography. *Phys. Fluids*, 19:085108, 2007.

[36] A. Chatterjee. An introduction to the proper orthogonal decomposition. *Current Science*, 78:808–816, 2000.

[37] A. K. Prasad, R. J. Adrian, C. C. Landreth, and P. W. Offutt. Effect of resolution on the speed and accuracy of particle image velocimetry interrogation. *Exp. Fluids*, 13:105–116, 1992.

[38] J. Westerweel. Fundamentals of digital particle image velocimetry. *Meas. Sci. Tech.*, 8:1379–1392, 1997.

[39] K. T. Christensen. The influence of peak-locking errors on turbulence statistics computed from piv ensembles. *Exp. Fluids*, 36(3):484–497, 2004.

[40] S. M. Soloff, R. J. Adrian, and Z. C. Liu. Distortion compensation for generalized stereoscopic particle image velocimetry. *Meas. Sci. Tech.*, 8:1441–1454, 1997.

[41] B. Wieneke. Stereo-PIV using self-calibration on particle images. *Exp. Fluids*, 39:267–280, 2005.

[42] N.G. Deen, P. Willems, M. van Sint-Annaland, J.A.M. Kuipers, R.G.H. Lammertink, A.J.B. Kemperman, M. Wessling, and W.G.J. van-der Meer. On image pre-processing for piv of single- and two-phase flows over reflecting objects. *Experiments in Fluids*, pages 1–6, 2010.

[43] S. S. Lu and W. W. Willmarth. Measurements of the structure of the Reynolds stress in a turbulent boundary layer. *J. Fluid Mech.*, 60:481–511, 1973.

[44] S. Nakagawa and T. J. Hanratty. Particle image velocimetry measurements of flow over a wavy wall. *Phys. Fluids*, 13(11):3504–3507, 2001.

[45] J. Zhou, R. J. Adrian, S. Balachandar, and T. M. Kendall. Mechanisms for generating coherent packets of hairpin vortices in channel flow. *J. Fluid Mech.*, pages 353–396, 1999.

[46] R. J. Adrian, C. D. Meinhart, and C. D. Tomkins. Vortex organization in the outer region of the turbulent boundary layer. *J. Fluid Mech.*, 422:1–54, 2000.

[47] B. Ganapathisubramani, N. Hutchins, W. T. Hambleton, E. K. Longmire, and I. Marusic. Investigation of large-scale coherence in a turublent boundary layer using two-point correlations. *J. Fluid Mech.*, 524:57–80, 2005.

[48] Y. Wu and K.T. Christensen. Spatial structure of a turbulent boundary layer with irregular surface roughness. *J. Fluid Mech.*, (in press):1–37, 2010.